

Deformation enduring conveyance of structured light through multimode waveguides and its exploitation for flexible hair-thin endoscopes

Sergey Turtaev^{1,†}, Tomáš Tyc^{2,3,†} Ulf Poßner⁴, Tina Eschrich¹, Torsten Poßner⁴, Yang Du¹, André Gomes¹, Bernhard Messerschmidt⁴, and Tomáš Čižmář^{1,2,5,*}

Abstract

The remarkable advancements in our capacity to synthesise structured light have facilitated the generation of any desired optical landscapes and even controlling the spatial distribution of light propagating through optically complex media such as multimode fibres. The availability of precisely defined structured light at the extremity of an exceedingly narrow and flexible cable holds the potential to stimulate a diverse range of highly sought-after applications, encompassing rapid communication, quantum computing, and, notably, imaging. What we lack in reaching these aspirations is the resilience of such light transport to deformations of the waveguide. Although recent theoretical investigations have delineated the attributes of ideal multimode fibres capable of deformation-enduring conveyance of structured light, tangible fibres possessing this indispensable trait to a practical extent remain elusive. Our study takes a deep dive into the precision of commercially available multimode fibres with the highest probability of demonstrating the phenomenon. We identified minuscule imperfections in their refractive index distribution, examined how these affect light transport when the fibre is deformed, and studied their implications for imaging applications. Our investigation has confirmed that these imperfections are indeed responsible for the undesirable alterations introduced into the output structured light fields during bending. Finally, as an alternative to standard graded-index fibres, manufactured by drawing silica-based preforms, we present narrow multimode waveguides in which the refractive-index profile has been established by ion exchange. These waveguides indeed exhibit previously unseen resilience of structured light transport even under severe deformation conditions and aptly fulfil the requirements of imaging applications.

Keywords

multimode fibre, transformation matrix, endoscopy

¹Leibniz Institute of Photonic Technology, Albert-Einstein-Straße 9, 07745 Jena, Germany

²Institute of Scientific Instruments of CAS, Královopolská 147, 612 64, Brno, Czechia

³Department of Theoretical Physics and Astrophysics, Faculty of Science, Masaryk University, Kotlářská 2, 61137 Brno, Czech Republic

⁴GRINTECH GmbH, Schillerstraße 1, 07745 Jena Germany

⁵Institute of Applied Optics, Friedrich Schiller University Jena, Fröbelstieg 1, 07743 Jena, Germany

[†]Authors contributed equally

^{*}Corresponding author: tomas.cizmar@leibniz-ipht.de

Introduction

The recent explosion of research activity in the domain of structured light has already witnessed an impact across disciplines. The 2014 Nobel prize in Chemistry for the development of super-resolved fluorescence microscopy is probably the most famous example and numerous research and industrial applications nowadays emerge with steadily increasing pace. While we are able to routinely synthesise highly complex and vector structured light fields with millions of degrees of freedom, we lag behind in translating them from our bulky, table-top geometries into compact and integrated solutions and in their delivery to where they are needed. Exploiting multimode fibres (MMFs) to deliver structured light towards its application site or to convey it between remote sites of an optical system, could greatly accelerate these prospects. Methods to counteract the transformation of a structured light, which it

experiences during propagation in a MMF, became very popular research domain in the past decade [1–5]. MMFs are commonly considered as a special class of complex media. Transport of coherent light signals through them can therefore be described in conveniently chosen representation of light modes as a linear operator commonly referred to as the transmission matrix (TM) [6]. This relationship between input and output of the fibre must be known prior a system utilising MMF can be used for synthesis of desired structured light outputs. In most cases it is obtained empirically in procedure referred to as the calibration [7]. As the calibration takes place, one needs full optical access to both ends of the MMF segment and it typically involves sequential propagation of a complete basis of input modes through the MMF while monitoring the output fields with the use of interferometry. When the TM becomes available, one can synthesise any desired optical field at the output (distal) end by generating the

corresponding input field and coupling it into the input (proximal) end of the MMF. The optimal results are reached when one controls the spatial distribution of all aspects of the input field including its amplitude, phase and polarisation [8]. Even in the highest performing systems reported so far, the calibration can be completed in a few minutes. Arguably, the highest application potential of this approach has been found in imaging. The unparalleled information density of MMFs allows them to convey images through hair-thin instruments having orders of magnitude smaller footprint when compared to other established technologies. Advanced geometries have already enabled deep-tissue observations of fluorescently labelled neurones in living animal models [9–12], label-free non-linear imaging of biological tissues [13], minimal access observations of macroscopic objects [14] which was also combined with time-of-flight based 3D reconstruction [15]. Further applications beyond imaging include delivery of structured light forming dynamic 3D holographic optical tweezers [16] and micro-manufacturing [17–19].

With the calibration procedure completed, the application relying on delivery of a structured light can proceed in principle indefinitely, as long as the layout of the fibre remains unchanged. Initial experiments have shown that the geometries might tolerate a small amount of MMF bending, stronger MMF deformations have, however, resulted in significant changes to the TM and a fresh calibration was required to retain the original performance. This constraint to stationary MMF geometries has been seen as the most significant drawback of this perspective method from its inception. The exemplar case of *in-vivo* neuroscience would greatly benefit from the possibility of deep-tissue minimum access observations in brains of fully functioning motile animal models, yet because of this very problem, all uses of MMF-based imaging demonstrations have been restricted to immobilised animals under anaesthesia where important processes behind neuronal signalling are significantly suppressed or completely silenced. This, combined with analogous desires within numerous other application areas has triggered the attention of many, who within the recent years have attempted to provide a solution. One group of possible strategies explore the growing power of computing and electronics. These involve repeated calibration for all intended fibre layouts upfront [20, 21], predicting changes to TM based on the observed fibre layout [22], eliminating the need for optical access to the MMF's distal end [21, 23–25] and the exploitation of deep learning [26–28].

Separate efforts concentrated on the MMF itself. It has been identified very early that TMs of different kinds of MMFs from various manufactures exhibit very different level of resilience to bending [29]. Broader theoretical insight into light transport through MMFs have predicted that graded index fibres following perfectly parabolic distribution of the square of the refractive index (n^2) across its core shall feature the most deformation-enduring conveyance of structured light (DECStL) [30]. The phenomenon of DECStL can be best outlined when considering photons as particles. The specific distribution of refractive index profile forms a harmonic potential well [31] while a bend of the fibre provides

linear potential slant. A photon moving inside an adiabatically curved fibre thereby still experiences almost identical harmonic potential well, albeit slightly shifted towards the outer side of the bend. Its evolution therefore does not deviate from that in a straight fibre. With the steep progress in quality of commercially available graded index fibres, namely the recent introduction of the OM5 standards (where the extended bandwidth indicates ever-highest precision in the refractive index distribution), several crucially important questions arise: To what extent is DECStL available in fibres commercially available nowadays? What precision would be required to meet the application demands without compromises? Can better-performing fibres be produced by any currently available technology? In this paper we consolidate all necessary requisites to answer these questions.

We quantify deviations from the ideal parabolic refractive index distributions across a spectrum of the most promising commercially available candidates within our reach. We develop rigorous theoretical model predicting light transport through such aberrated fibres and simulate their imaging performance under bending deformations. Further, by benchmarking these predictions against the direct experimental reality, we confirm that minuscule manufacturing aberrations, typically in the order of 10^{-5} – 10^{-4} , are indeed to blame for the changes to the TM induced by fibre bending.

Most importantly we propose and implement alternative manufacturing approach based on ion exchange [32], which is expected to improve the precision of refractive index distribution and reach characteristics more favourable for bending resilience when compared to standard graded-index fibre manufacturing methods. The novel waveguides have been designed to allow propagation of ≈ 17 000 modes, which could be used to convey images with the ever-highest pixel resolution [25]. The resulting products, referred to here as the DECStL waveguides exhibit minimal imaging performance degradation even when deformed all the way towards their damage limits, which contrasts widely with the results achieved while using commercially available fibres.

Results

For the experimental studies, six most promising commercially available candidates for bending-resilient fibre, featuring different core sizes and numerical apertures, have been selected based on our market research. Their identifiers in this work ($GI_{S/M/L}^{1/2}$), manufacturers and specifications are explained in supplementary materials (SM, table S1). This selection has been complemented by a step-index fibre (SI) which has been most commonly used in previous experimental work on this topic.

The last candidate to be assessed for its bending resilience is the newly developed DECStL waveguide. A cane from alumino-boro-silicate glass [33] has been drawn in an in-house fibre-drawing tower into the diameter 125 μm (matching that of all the fibres used) and subjected to ion exchange as detailed in SM, aiming to produce parabolic distribution of n^2 giving the NA of 0.5. The available ion-exchange reactor has enabled lengths of up to 54 mm, therefore all candidates have been tested at matching

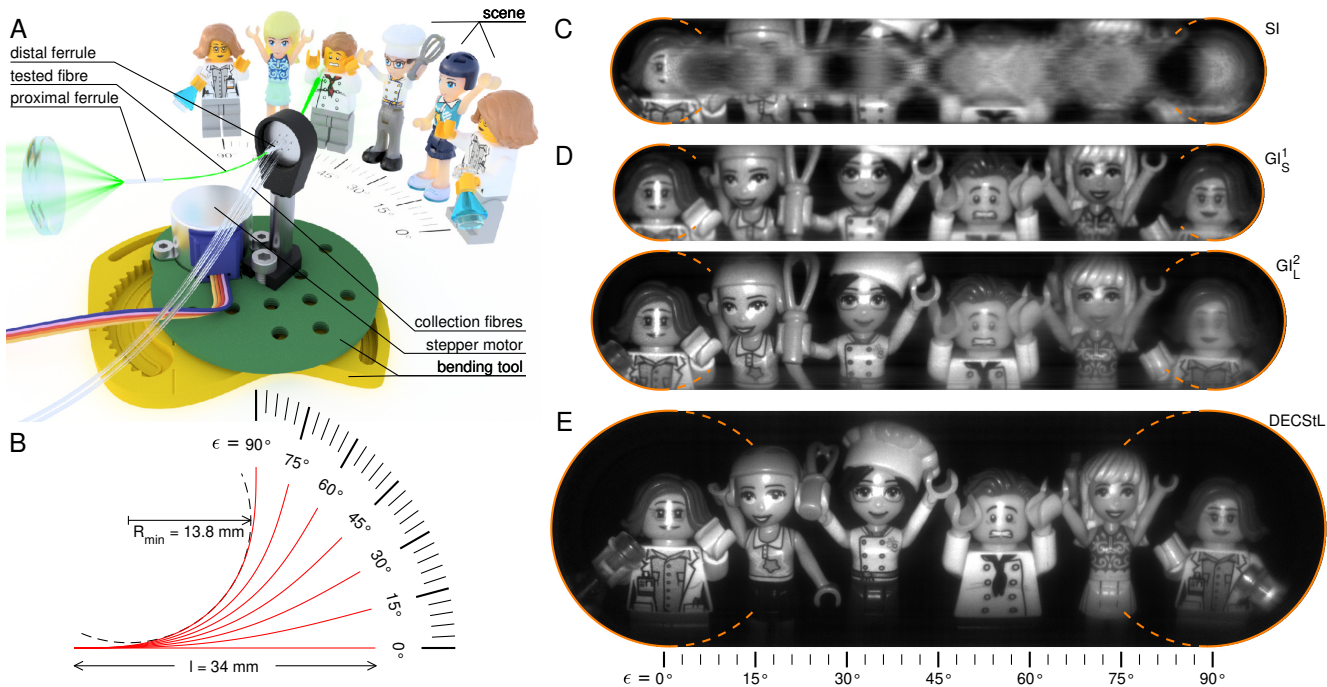


Fig. 1. Qualitative illustration of bending resilience. (A) Bending tool translating and reorienting the distal end imposing adiabatic curvature along the used fibre. (B) Range of adiabatic fibre layouts used. (C) Scene recorded by SI fibre. The central part is obtained by combining narrow middle sectors (5 pixels wide) of images obtained as the fibre was bend across the full range of the bending tool. Half-moon parts at the left and the right are taken from the first and the last recorded image respectively. (D) Scene recorded by the best performing commercially available graded-index fibres of our selection and the best roll orientation, with the lowest and the highest information capacity (GI_S^1 and GI_L^2). (E) Scene recorded by DECSiL waveguide for its full information capacity. Roll orientation played no observable role.

length.

For all experiments we use the geometry of the far-field holographic endoscope [14, 15], detailed in SM. It has been optimised to adapt to optical fibres with core size ranging from $50 \mu\text{m}$ to $125 \mu\text{m}$ and NAs between 0.2 and 0.5.

In all our studies the fibre's TM was measured at the initial, almost straight layout. A small contortion (negligible with respect to other bent layouts under investigation) has been allowed to avoid stretching the fibre at this layout. The instrument is equipped with custom-made bending tool, which has been designed to introduce strictly adiabatic bending deformation to the 34 mm long segment of the used fibre (remaining length when using two 10 mm long termination ferrules) by simultaneous positioning and orienting of the distal end. While there are numerous other possible parametrisable layouts of the fibre, which can be introduced by positioning and orienting the segment's ends, the adiabatic shape featuring smooth curvature and its first derivative is the only one that requires no torques applied to the ends (see SM for details) and therefore it is the easiest shape to reproduce without imposing other means of deformations such as local stress. Following the TM measurement, the bending tool has been employed. It introduces any bend ranging from the initial (calibrated) layout and the terminal layout with the distal end yaw (ϵ , angle of the distal end axis measured from the proximal end axis) reaching 90° and extreme radius of curvature reaching 13.8 mm (see Fig.

1B). Imaging is achieved through point-by-point scanning of a diffraction-limited spot over the objects within the field of view, while collecting the back-scattered light intensity by additional fibres. As discussed elsewhere [14], it is very challenging to implement both, object illumination and collection of returning signals through the same fibre in the far-field reflectance geometry, mainly due to overwhelmingly strong reflections at the facets and scattering at defects of the fibre. The issue vanishes when imaging in close proximity of the distal end as well as while employing fluorescence-based [12] or non-linear [34] imaging approaches where respective excitation and signal collection optical pathways can be separated spectrally. While previous works used the narrowest possible collection fibres in the closest possible proximity of the illumination waveguide in order to maintain minimal dimensions of the instrument, our experiment settings are optimised purely for studies of the bending resilience. Therefore we include six step-index collection fibres of much larger cores ($400 \mu\text{m}$) and NAs (0.5), each displaced several millimetres from the illumination fibre under investigation. Next to considerably stronger signals, this solution does not affect the fibre layout and avoids image contamination by speckle artefact originating from the coherent nature of the signal [14].

Prior to our detailed quantitative assessment of the bending resilience we provide a qualitative demonstration of all used fibre types by capturing the same scene while increasing the distal end

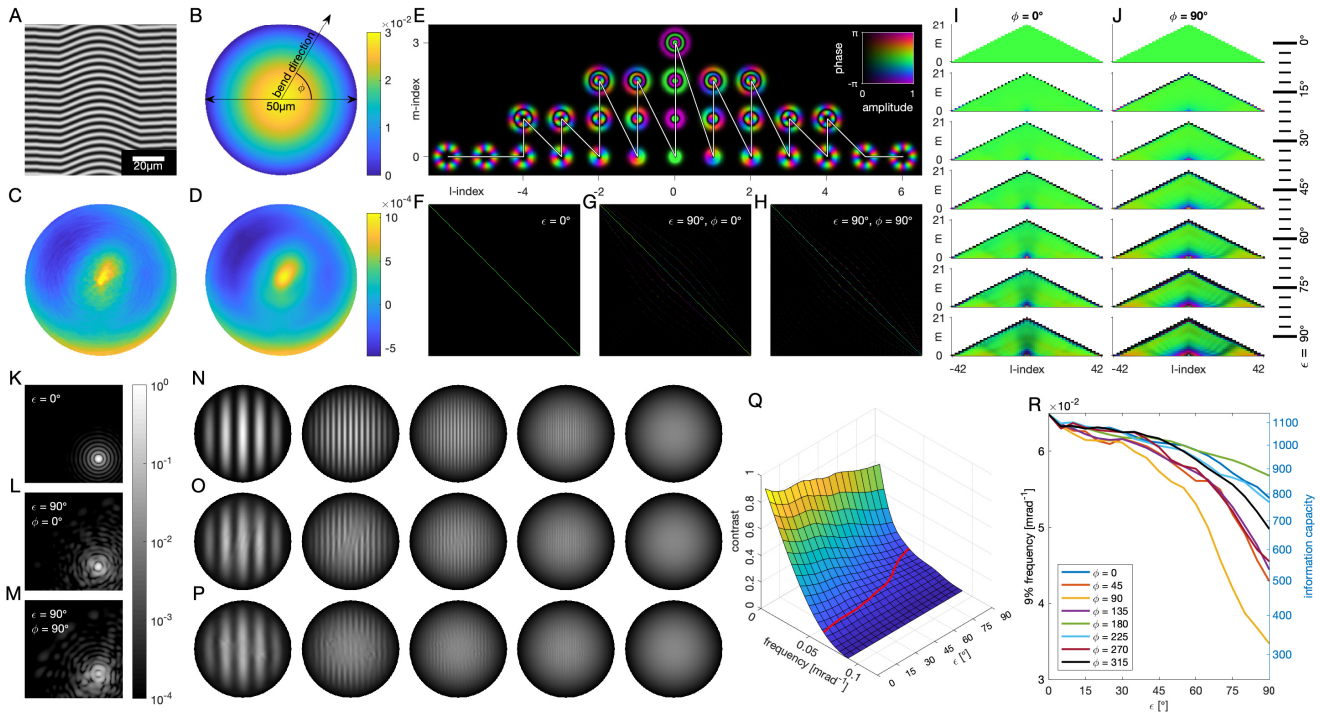


Fig. 2. Imaging performance bending resilience modelling for aberrated fibres. GI_M^2 is used as model case for all data shown in this figure. (A) Interferogram of fibre placed perpendicularly with respect to the object wave direction. (B) Computer tomography-based reconstruction of refractive index difference from that of the cladding material. (C) Isolated aberration after paraboloid dependence has been subtracted. (D) Aberration after low-pass filtering by projection onto 300 lowest Zernike polynomials. (E) PIMs of perfect parabolic fibre. Solid line indicates their order considered in deformation operators below. (F to H) DOs for straight fibre (unitary matrix) and two cases bent fibre (distal yaw of 90°) for different roll orientations. For better clarity the basis in these examples has been reduced to 320 PIMs of the lowest order (largest propagation constants), where the strongest effects of bending appear. (I and J) Diagonal components of complete DOs organised into mode pyramids (as in D) for two different roll orientations and gradually increasing distal end yaw. (K to M) Examples of far-field foci formed through deformations of F to H, considering the fibre was calibrated at the straight layout. (N to P) Simulated raster-scanning-based imaging of single-spatial-frequency gratings for corresponding deformations. (Q) Contrast transfer function evolution under the influence of bending. Values of contrast were averaged over the field of view and four different orientations of the grating's fringes. The red contour signifies the resolution limiting 9% frequency (analogous to Rayleigh criterion). (R) 9% frequency and total information capacity dependence on the distal end yaw for several different roll orientations of the fibre.

yaw (see Fig. 1A). In most commercially available fibres the refractive index aberrations are not azimuthally independent, which results in significantly diverse bending resilience for different roll orientations of the fibre (ϕ). In Supplementary movie SM1, we provide records of the scene during progressive bending for the worst as well as the best performing roll orientation. The DECSiL waveguide exhibited no significant differences for different roll orientations, therefore only one orientation is provided. The study however includes imaging results for reduced information capacities (virtually reducing the NA and the core size of the in-coupled signal) to allow performance comparison with the commercial fibres. A selection of the results is visualised in Fig. 1, for the step-index fibre (Fig. 1C), two examples of the commercial fibres performing at the lowest and the highest information capacities available, both at their best-performing roll orientation (Fig. 1D), and the DECSiL waveguide at its full capacity (Fig. 1E).

Our quantitative investigation is conceived to provide the rigorous explanation for the light transport changes and the image degradation under the influence of bending. The hypothesis, which we put forward for the observed lack of robust bending resilience in common graded-index fibres is the presence of perturbations in their refractive index profile. In the following, we therefore measure the refractive index profile, predict the bending resilience by a numerical model and compare the result with the experimental reality.

The refractive index profile (its difference from the cladding material) is acquired by the means of computer tomography, using records from multidirectional interferometric measurements (see Fig. 2A for an example of an interferogram acquired and SM for further details). Subtracting the ideal fibre profile of the optimum fit for the centre of symmetry and NA reveals the identified aberrations (see Fig. 2C), exhibiting visible high-frequency

wavelets. Using the raw data in our numerical model resulted in much stronger inter-mode coupling than that observed in our experiments, therefore we assumed that the high frequency wavelets represent numerical artefacts of the computer tomography procedure. We therefore low-pass filtered the measurements by decomposition into the Zernike polynomials defined at the area of the fibre core (value given by manufacturer's specifications) and use only these of the first 24 orders (300 elements, see Fig. 2D), which represents the largest possible threshold before the high-frequency artefacts start to emerge. The measurement results from all the used fibres are presented in SM.

Our numerical model to predict the light transport through perturbed fibres assumes that the refractive index distribution is close to the ideal shape, featuring an arbitrary but relatively small perturbation, which does not change along the fibre's axis. The model is built upon the identification of modes in uniformly bent and perturbed fibres, with the transmission through arbitrarily curved fibres being realised in discrete segments, in each of which the curvature can be regarded as essentially uniform. The modes of the perturbed fibre are expressed as a superposition of the propagation invariant Laguerre-Gaussian modes (PIMs, see Fig. 2E) of the unperturbed fibre. The model is detailed in supplementary information, together with discussions about its most important predictions. These include the realisation that perturbations which are symmetric with respect to the fibre axis (point symmetry of refractive index cross-section) cause much weaker changes to light transport when compared to the antisymmetric ones. Further, the model predicts that the influence of any given perturbation grows proportionally to fibre diameter and it falls with the square of the NA. The result of the model is a deformation operator (DO), which is defined as a matrix, with which one must multiply the TM of the straight fibre in order to obtain that of the bent fibre. Figs. 2G and 2H exemplifies DOs in their matrix form, while Figs. 2I and 2J show evolution of the DO's diagonal components (PIMs) under the influence of increasing amount of bending for two different roll orientations of the fibre. To predict the imaging performance, we simulate imaging by virtually exposing grating targets of varying spatial frequencies (sinusoidal) by sequence of farfield foci, one for each desired pixel. For each we identify the superposition of PIMs which is to be coupled into the straight fibre in order to achieve the desired diffraction-limited focus (see Fig. 2K). Analogous illumination fields of the bent fibre is obtained by multiplying the same vector of PIMs with DO calculated by our theoretical model for the actual fibre layout (see Figs. 2L and 2M). Each pixel of the resulting image is obtained as the inner product of the intensity distribution of the corresponding focus with the grating target (see figs. 2 n-p). An example of contrast of the resulting images, averaged over the field of view and four different orientations of the grating targets is presented in Fig. 2Q as a function of the target's spatial frequency and the amount of bending. Following the Rayleigh definition of resolution, we consider the limiting spatial frequency at the contrast level of 9% [14]. The total number of resolvable features (information capacity) can be estimated as square of the limiting

frequency multiplied by the area of the field of view. These quantities are presented in Fig. 2R for 8 different roll orientations of the fibre.

Finally we provide direct experimental evidence quantifying the fibres' bending resilience. The bending tool was equipped with holder carrying frequency targets, which are kept stationary with the distal end of the used MMF (see Fig. 3A). The square (Ronchi) targets of various frequencies are printed by black ink on a white paper and glued onto magnetic frames allowing four different orientations of the fringes with respect to the system. Following the calibration at the initial close-to-straight layout of the fibre the system provides images along the full interval of adiabatic contortions for variety of spatial frequencies and four orientations of the fringes (see Fig. 3B and 3C for examples). The measurements were repeated for six roll orientations of the used fibre and all fibres considered. Analogously to the previous simulation approach, the images are used to quantify the contrast. There are three experimental issues, influencing the measured values of contrast. First, due to presence of noise in TM measurement and the used light-modulation mechanism, our diffraction-limited foci contain only around 70% of the total transmitted power, the fraction varies for different fibres with the dimension of their TMs. The remaining power is distributed in the form of speckled background across the field of view. Further, the black ink is not perfectly absorbing. Lastly, the Ronchi targets used had square rather than sinusoidal reflectivity cross-section. In all the cases, however the contrast, obtained from the Fourier transform of the image, was affected for all frequencies of the same dataset by the same factor. The results are therefore normalised, demanding to reach unity when extrapolating the obtained dependency for of the initial layout to the spatial frequency of zero (see Fig. 3C) as expected in the case free from the above experimental issues.

The side-by-side comparison of the obtained results is summarised in Figs. 3E to 3G in the form of information capacity reduction under the influence of bending. The shaded areas represent confidence intervals (\pm one standard deviation) for results obtained at different roll orientations while the solid lines show the average. The simulations, which closely followed the experimental conditions (see Fig. 3E), could only be completed for four fibres of the low and medium information capacity as the available computing power (96 CPU cores, 2TB memory) was insufficient to handle larger datasets efficiently. The step-index fibre was also not simulated as the difference of the step-index refractive index profile from the ideal paraboloid is too high to be considered as a perturbation. Yet, direct comparison with the experimental results shown in Fig. 3F reveals very similar trends for the corresponding fibres in both, the mean values and the variations across different roll orientations. Clearly, GL_S¹ (Draka WideCap-OM5) exhibits the highest bending resilience, which corresponds well with the qualitative impressions introduced earlier. Unfortunately, it offers only a very small information capacity. Higher-capacity commercial fibres exhibit much steeper performance degradation under equivalent bending. Analogous measurements of the DECstL waveguide shown in Fig. 3G however reveal immensely enhanced

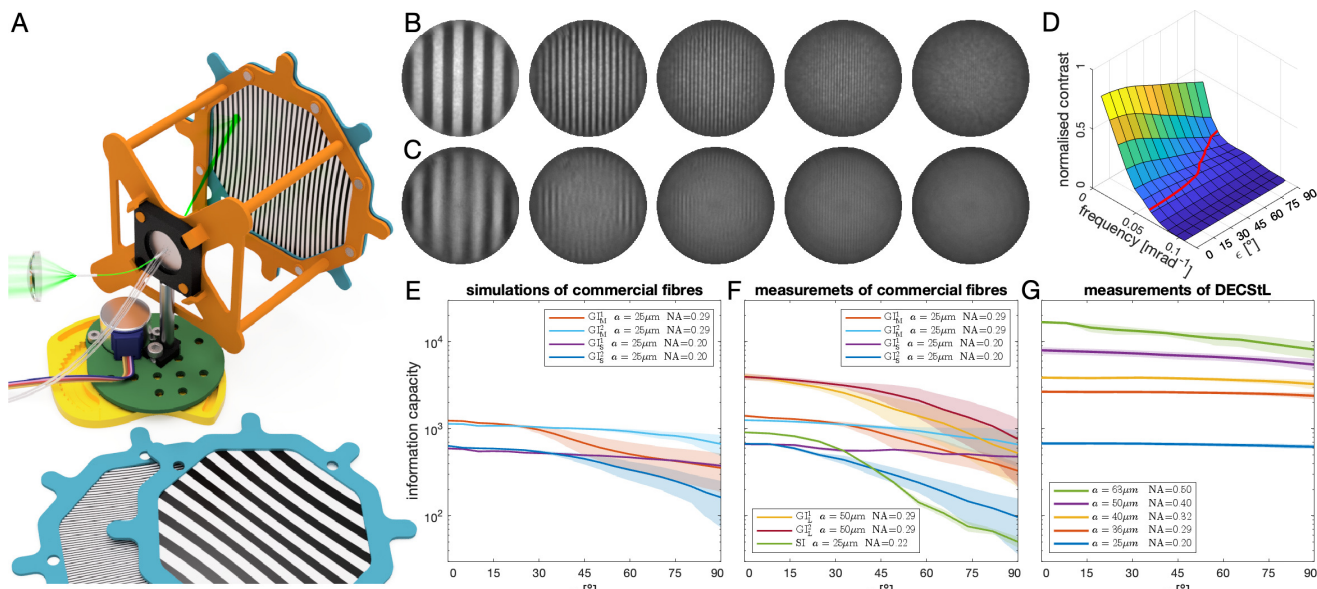


Fig. 3. Experimental assessment of imaging performance resilience to bending and its comparison to theoretical prediction. GI_M^2 is used as model case for results shown in panels A to C. (A) Illustration of experimental settings and procedure. (B and C) Raw images of Ronchi targets obtained for straight and bent (90° distal yaw) fibre layouts respectively. (D) Normalised contrast transfer function evolution under the influence of bending. The red contour signifies the resolution limiting 9% frequency. (E) Modelled decline of total information capacity (number of resolvable features) under the influence of bending for four fibres which our model could handle. Shaded intervals signify spread obtained for different roll orientations. (F) Corresponding experimental results for the same fibre selection as in E, with additional fibres of higher capacity and the step-index type. (G) Equivalent measurements on DECStL waveguide with information capacity of the initial layout manipulated by aperturing the input signals.

bending resilience, greatly outperforming the best tested commercial fibre even when used to convey orders of magnitude larger amount of imaging information.

Discussion

In summary, our studies show that, with sufficiently precise profile of refractive index distribution, deformation-enduring conveyance of structured light through multimode fibre optics can be reached to unprecedented levels.

The work provides detailed analysis of refractive index perturbations seen in commercially available graded-index fibres and it links them with the undesired changes to light transport taking place while fibre bending. Our theoretical model, verified by direct comparison with the experimental reality allows one to predict bending-resilience of a given fibre, based purely on the knowledge of its refractive index profile. The model predicts that symmetric and antisymmetric perturbations have starkly contrasting influence of light transport, which brings about interesting implications for the fibre manufacturing processes. To appreciate its importance, consider the example of GI_s^1 and GI_s^2 , which have a very similar parameters and also the refractive index perturbations. Yet GI_s^1 features slightly asymmetric profile with respect to the axis, while GI_s^2 is almost perfectly symmetric (see supplementary figure S3). Yet, both the numerical model-based prediction and the experimental reality concordantly exhibit very differing

bending resilience outcomes for these fibres. Investing effort to eliminating all radially symmetric perturbations but also the ellipticity of the fibre is therefore not advisable when striving to improve the bending resilience, one should rather focus mainly on making the production process as symmetric with respect to the fibre axis as possible. Further, the model predicts that same perturbation may affect the bending resilience very differently shall it be present on fibres with different core size and NA. The most simple way to support bending resilience in practical cases is to opt for the highest NA fibre with the smallest possible size of its core. These considerations allows us to define a simple quantity which is available purely from the RI profile measurement. The bending resilience predictor (BRP), introduced in SM (Materials and Methods, part 7) it is insensitive to fibre parameters and it can serve as a rough indication whether or not the waveguide in question is suitable as bending resilient medium. The relative information capacity of the bent waveguides (related to the performance of the original straight fibre for which the TM has been acquired), as a function of BRP, is shown in SM (supplementary figure S7) for all our experimental results and simulations. We believe that more robust version of this study could soon form the basis for a wide-spread quality standard to describe MMF bending resilience.

Despite a very satisfying prognosis on bending resilience, a notable disparity exists between the model's projections and

the empirical findings. The model anticipates the preservation of circular polarization state in light propagation, both within straight and bent fibre configurations. This has been empirically validated in step-index fibers [22], however, graded-index fibres exhibit a distinct response, resulting in the complete randomisation of polarisation states at the output. The underlying mechanisms for this dissimilarity remain unclear, and it will be a subject of our future research agenda.

We present novel approach for manufacturing flexible multimode waveguides based on ion exchange, providing very high degree of bending resilience and simultaneously featuring very high information capacities, combination of which significantly exceeds that of commercially available competitors. As seen in the measurements of refractive index profiles, its absolute perturbation is comparable to that found in the best-performing commercial fibres. Yet, as we explain in SM (Materials and Methods, part 3), their magnitude must be weighted against the square of the NA in order to predict their bending resilience. The success of the DECStL waveguide therefore results from both, the low perturbations and the significant NA enhancement, both enabled by the ion-exchange process.

Our work is likely to rise numerous questions which cannot be answered within the scope of this paper at the depth of the above presented results. Yet there are several important findings which are worth outlining:

As we performed our studies with relatively short fibre segments, it is desirable to know how the bending resilience translates to longer ones. In order to provide an initial insight, we provide comparable study at 150 mm long fibre segment in SM (Materials and Methods, part 11) and showcase imaging of a scene with 1 m long fibres in Supplementary Movies SM2 and SM3. These results clearly show that bending resilience is significantly enhanced for longer fibres whose distal end reaches a certain yaw angle along paths or smaller curvature.

Our study has not covered twisting deformations in detail. We argue that most of conceivable applications could be engineered minimising the need for twist deformations, therefore it is of much lower importance when compared to bending. When applying a similar derivation approach to the one used for analysing the effects of bending on perturbed fibres, one might find that dependence on core size and NA holds also for twist deformations, but the significance of symmetric and antisymmetric perturbations reverses. Our supplementary movie SM4 shows that small amount of twist affects the DECStL waveguide's performance minimally, while it can play a profound role in commercial fibres.

We anticipate that a novel class of multimode waveguides, capable of achieving or surpassing the performance demonstrated by the DECStL waveguide described herein, will have broad applications across diverse research and industrial sectors. Spatially structured light fields play a crucial role in numerous manufacturing processes, demanding meticulous attention to maintaining the alignment of individual components. By constructing optical pathways with components that can be macroscopically translated without impacting the resulting structured fields, substan-

tial reductions in system complexity and costs may be realized. Telecommunications, in particular, stands to benefit significantly from the utilisation of bending-resilient fibers, enhancing spatial domain multiplexed data transfer. Additionally, within the realm of quantum computing, DECStL MMFs will facilitate the delivery of quantum optical states between remote processing units. Primarily motivated by imaging applications, our work foresees that the adoption of DECStL waveguides will address the most significant limitation of MMF-based holographic endoscopes. This breakthrough paves the way for their rapid integration into various promising fields, including *in-vivo* neuroscience. In this context, these fibers offer the unprecedented capability to enable high-resolution structural imaging of deep-seated brain structures in motile and behaving animal models. We anticipate that our work will stimulate fibre producers to include the BRP or other unified DECStL quantifying standard of their products amongst their specifications and focus on development of new, further empowered DECStL waveguides.

References

- [1] Bianchi, S. & Di Leonardo, R. A multi-mode fiber probe for holographic micromanipulation and microscopy. *Lab Chip* **12**, 635–639 (2012).
- [2] Čižmár, T. & Dholakia, K. Exploiting multimode waveguides for pure fibre-based imaging. *Nature Communications* **3** (2012).
- [3] Choi, Y. *et al.* Scanner-free and wide-field endoscopic imaging by using a single multimode optical fiber. *Phys. Rev. Lett.* **109**, 203901 (2012).
- [4] Papadopoulos, I. N., Farahi, S., Moser, C. & Psaltis, D. High-resolution, lensless endoscope based on digital scanning through a multimode optical fiber. *Biomed. Opt. Express* **4**, 260 (2013).
- [5] Plöschner, M. *et al.* Multimode fibre: Light-sheet microscopy at the tip of a needle. *Scientific Reports* **5**, 18050 (2015). URL <http://www.nature.com/articles/srep18050>.
- [6] Popoff, S. M. *et al.* Measuring the transmission matrix in optics: An approach to the study and control of light propagation in disordered media. *Phys. Rev. Lett.* **104**, 100601 (2010).
- [7] Čižmár, T. & Dholakia, K. Shaping the light transmission through a multimode optical fibre: Complex transformation analysis and applications in biophotonics. *Optics Express* **19** (2011).
- [8] Gomes, A. D., Turtaev, S., Du, Y. & Čižmár, T. Near perfect focusing through multimode fibres. *Opt. Express* **30**, 10645–10663 (2022). URL <https://opg.optica.org/oe/abstract.cfm?URI=oe-30-7-10645>.
- [9] Ohayon, S., Aguirre, A. M. C., Piestun, R. & DiCarlo, J. J. Deep brain fluorescence imaging with minimally invasive ultra-thin optical fibers. *bioRxiv* (2017).

- [10] Turtaev, S. *et al.* High-fidelity multimode fibre-based endoscopy for deep brain *in vivo* imaging. *Light: Science & Applications* **7**, 92 (2018). URL <https://doi.org/10.1038/s41377-018-0094-x>.
- [11] Vasquez-Lopez, S. A. *et al.* Subcellular spatial resolution achieved for deep-brain imaging *in vivo* using a minimally invasive multimode fiber (2018).
- [12] Stiburek, M. *et al.* 110 μm thin endo-microscope for deep-brain *in vivo* observations of neuronal connectivity, activity and blood flow dynamics. *Nature Communications* **14**, 1897 (2023). URL <https://doi.org/10.1038/s41467-023-36889-z>.
- [13] Cifuentes, A. *et al.* Polarization-resolved second-harmonic generation imaging through a multimode fiber. *Optica* (2021).
- [14] Leite, I. T., Turtaev, S., Boonzajer Flaes, D. E. & Čižmár, T. Observing distant objects with a multimode fiber-based holographic endoscope. *APL Photonics* (2021). 2011.03600.
- [15] Stellinga, D. *et al.* Time-of-flight 3d imaging through multimode optical fibers. *Science* **374**, 1395–1399 (2021). URL <https://www.science.org/doi/abs/10.1126/science.abl3771>. <https://www.science.org/doi/pdf/10.1126/science.abl3771>.
- [16] Leite, I. T. *et al.* Three-dimensional holographic optical manipulation through a high-numerical-aperture soft-glass multimode fibre. *Nature Photonics* (2018).
- [17] Morales-Delgado, E. E. *et al.* Three-dimensional microfabrication through a multimode optical fiber. *Optics Express* **25**, 7031–7045 (2017).
- [18] Delrot, P., Loterie, D., Psaltis, D. & Moser, C. Single-photon three-dimensional microfabrication through a multimode optical fiber. *Optics Express* **26**, 1766–1778 (2018).
- [19] Konstantinou, G. *et al.* Improved two-photon polymerization through an optical fiber using coherent beam shaping. *Optics and Lasers in Engineering* **160**, 107232 (2023).
- [20] Farahi, S., Ziegler, D., Papadopoulos, I. N., Psaltis, D. & Moser, C. Dynamic bending compensation while focusing through a multimode fiber. *Opt. Express* **21**, 22504–22514 (2013). URL <https://opg.optica.org/oe/abstract.cfm?URI=oe-21-19-22504>.
- [21] Wen, Z. *et al.* Single multimode fibre for *in vivo* light-field-encoded endoscopic imaging. *Nature Photonics* **17**, 679–687 (2023). URL <https://doi.org/10.1038/s41566-023-01240-x>.
- [22] Plöschner, M., Tyc, T. & Čižmár, T. Seeing through chaos in multimode fibres. *Nature Photonics* **9** (2015).
- [23] Gordon, G. S. D. *et al.* Characterizing optical fiber transmission matrices using metasurface reflector stacks for lensless imaging without distal access. *Phys. Rev. X* **9**, 041050 (2019). URL <https://link.aps.org/doi/10.1103/PhysRevX.9.041050>.
- [24] Li, S., Horsley, S. A., Tyc, T., Čižmár, T. & Phillips, D. B. Memory effect assisted imaging through multimode optical fibres. *Nature Communications* (2021). 2005.06445.
- [25] Li, S. *et al.* Compressively sampling the optical transmission matrix of a multimode fibre. *Light: Science and Applications* (2021). 2007.15891.
- [26] Fan, P., Zhao, T. & Su, L. Deep learning the high variability and randomness inside multimode fibers. *Opt. Express* **27**, 20241–20258 (2019). URL <https://opg.optica.org/oe/abstract.cfm?URI=oe-27-15-20241>.
- [27] Zhao, J. *et al.* High-fidelity imaging through multimode fibers via deep learning. *Journal of Physics: Photonics* **3**, 015003 (2021). URL <https://dx.doi.org/10.1088/2515-7647/abcd85>.
- [28] Abdulaziz, A., Mekhail, S. P., Altmann, Y., Padgett, M. J. & McLaughlin, S. Robust real-time imaging through flexible multimode fibers. *Scientific Reports* **13**, 11371 (2023). URL <https://doi.org/10.1038/s41598-023-38480-4>.
- [29] Loterie, D., Psaltis, D. & Moser, C. Bend translation in multimode fiber imaging. *Optics Express* **25**, 6263 (2017). URL <https://www.osapublishing.org/abstract.cfm?URI=oe-25-6-6263>.
- [30] Boonzajer Flaes, D. E. *et al.* Robustness of Light-Transport Processes to Bending Deformations in Graded-Index Multimode Waveguides. *Physical Review Letters* **120** (2018).
- [31] Leonhardt, U. & Philbin, T. *Geometry and light: the science of invisibility* (Courier Corporation, 2012).
- [32] Messerschmidt, B., Possner, T. & Goering, R. Colorless gradient-index cylindrical lenses with high numerical apertures produced by silver-ion exchange. *Appl. Opt.* **34**, 7825–7830 (1995). URL <http://www.osapublishing.org/ao/abstract.cfm?URI=ao-34-34-7825>.
- [33] Bernhard, M., Christian, R., Sandra, H., Torsten, P. & Ulf, P. Alumino-boro-silicate glass and process to make crystal-free gradient index lenses (2004). EP Patent, EP1544176A2.
- [34] Trägårdh, J. *et al.* Label-free cars microscopy through a multimode fiber endoscope. *Optics express* **27**, 30055–30066 (2019).

Supplementary Materials for

Deformation enduring conveyance of structured light through multimode waveguides and its exploitation for flexible hair-thin endoscopes

Sergey Turtaev[†], Tomáš Tyc[†], Ulf Poßner, Tina Eschrich, Torsten Poßner, Yang Du, André Gomes, Bernhard Messerschmidt, and Tomáš Čižmár
Correspondence to: tomas.cizmar@leibniz-ipht.de

This PDF file includes:

Materials and Methods
Figs. S1 to S9
Table S1
Captions for Movies SM1 to SM5
Caption for Data S1

Other Supplementary Materials for this manuscript include the following:

Movies SM1 to SM5
Data S1 to S2 [FibreBendingDesigns.zip, DataArchive.zip]

Materials and Methods

1. Finding modes of a bent GRIN fibre with a perturbation of the refractive index

In our experiments we used a GRIN fibre whose refractive index profile is close to the ideal parabolic one, but not perfect. The 2D index profile $n(x, y)$ in a selected cross section of the fibre was measured as explained in the main article, and the resulting squared profile was fitted by the ideal parabolic profile

$$n_{\text{id}}^2(x, y) = n_0^2 \left(1 - \frac{x^2 + y^2}{b^2} \right), \quad (S6)$$

where the parameters n_0 and b characterise the refractive index on the fibre axis and index steepness, respectively. The square of the measured 2D index profile can then be expressed as a sum of the ideal profile and the index perturbation

$$n^2(x, y) = n_{\text{id}}^2(x, y) + \Delta n^2(x, y). \quad (S7)$$

We want to describe light propagation in the fibre whose refractive index is perturbed like this and it is bent at the same time. To do so, we start from the exact equation for the transverse part of the electric field \mathbf{e}_t in a straight fibre¹

$$[\nabla_t^2 + k^2 n^2 - \beta^2] \mathbf{e}_t = -\nabla_t (\mathbf{e}_t \cdot \nabla_t \ln n^2), \quad (S8)$$

where ∇_t is the transverse nabla operator. In a bent fibre the local phase velocity of the wave is not constant throughout the fibre cross section but depends linearly on the distance from the centre of curvature^{1,2}. If we assume that the fibre is bent in the x direction and has curvature ρ , this corresponds to replacing β^2 in Eq. S8 by the expression $[\beta/(1 - \rho x)]^2 \approx \beta^2 + 2\beta^2\rho x$. In normal conditions, the second term $2\beta^2\rho x$ is smaller than the first term β^2 by several orders of magnitude. Then we can take advantage of the fact that the propagation constant of all the guided modes belong to a narrow range, $\beta \in (kn_{\text{cl}}, kn_0)$, where n_{cl} is the refractive index of the cladding. This enables to replace β in the second term by kn_0 , so we finally get $[\beta/(1 - \rho x)]^2 \approx \beta^2 + 2k^2 n_0^2 \rho x$. With this modification to Eq. S8 and upon employing Eq. S7, we get

$$[\nabla_t^2 + k^2(n_{\text{id}}^2 + \Delta n^2 - 2n_0^2 \rho x) - \beta^2] \mathbf{e}_t = -\nabla_t (\mathbf{e}_t \cdot \nabla_t \ln n^2). \quad (S9)$$

Next we expand the transverse field into a suitable basis of states. Such a basis can be derived from the basis of solutions of the scalar Helmholtz equation for the ideal parabolic index profile,

$$[\Delta_t + k^2 n_{\text{id}}^2 - \beta_{0i}^2] \psi_i = 0, \quad (S10)$$

where β_{0i} are the scalar propagation constants and ψ_i are the Laguerre-Gauss modes^{1,2}. The basis for the transverse electric field \mathbf{e}_t will then consist of the states ψ_i equipped with a unit polarisation vector $\hat{\mathbf{e}}_p$, where index p denotes one of two possible linear polarisation states $p \in \{x, y\}$. This way, we expand the field as

$$\mathbf{e}_t = \sum_{i=1}^N \sum_{p \in \{x,y\}} c_{ip} \psi_i(x, y) \hat{\mathbf{e}}_p, \quad (S11)$$

where N is the number of scalar modes that are guided by the fibre, so there are $2N$ states in our vector basis. Next we substitute this expansion into Eq. (S9), use Eq. (S10), multiply the resulting equation by $\hat{\mathbf{e}}_q \psi_j^*$, where $q \in \{x, y\}$ describes the linear polarisation we are projecting to, and integrate over the plane xy . Using in addition the orthonormality of the set of the scalar modes ψ_i , we get

$$\begin{aligned} c_{jq}(\beta_{0j}^2 - \beta^2) + \sum_i c_{iq} k^2 \int_{\mathbb{R}^2} \psi_j^* (\Delta n^2 - 2n_0^2 \rho x) \psi_i \, dx \, dy = \\ - \sum_{ip} c_{ip} \int_{\mathbb{R}^2} \psi_j^* \hat{\mathbf{e}}_q \cdot \nabla_t (\psi_i \hat{\mathbf{e}}_p \cdot \nabla_t \ln n^2) \, dx \, dy. \end{aligned} \quad (S12)$$

The next step is to simplify the integral on the right-hand side. For this purpose, to shorten the expressions, we introduce the scalar functions $P_{ip} = (\psi_i \hat{\mathbf{e}}_p \cdot \nabla_t \ln n^2)$, and write the integral as

$$\int_{\mathbb{R}^2} \psi_j^* \hat{\mathbf{e}}_q \cdot (\nabla_t P_{ip}) \, dx \, dy = \int_{\mathbb{R}^2} \nabla_t \cdot (\psi_j^* \hat{\mathbf{e}}_q P_{ip}) \, dx \, dy - \int_{\mathbb{R}^2} P_{ip} \nabla_t \cdot (\psi_j^* \hat{\mathbf{e}}_q) \, dx \, dy \quad (S13)$$

Next we take advantage of the fact that the integral over a 2D area A can be transformed into a line integral,

$$\int_A \nabla_t \cdot (\psi_j^* \hat{\mathbf{e}}_q P_{ip}) \, dx \, dy = \int_l (\psi_j^* \hat{\mathbf{e}}_q P_{ip}) \cdot \hat{\mathbf{n}} \, dl, \quad (S14)$$

see e.g. Eq. (37-55) of¹. Here the line l encircles the area A and $\hat{\mathbf{n}}$ denotes the unit outward normal to the line element dl . Now, expanding the area A to infinity, the line integral vanishes due to the exponential decay of the fields ψ_j and P_{ip} . This way, only the second term on the right-hand side of Eq. (S13) is nonzero. Substituting Eq. (S13) into Eq. (S12) then yields

$$\begin{aligned} c_{jq}(\beta_{0j}^2 - \beta^2) + \sum_i c_{iq} k^2 \int_{\mathbb{R}^2} \psi_j^* (\Delta n^2 - 2n_0^2 \rho x) \psi_i \, dx \, dy \\ - \sum_{ip} c_{ip} \int_{\mathbb{R}^2} \hat{\mathbf{e}}_q \cdot (\nabla_t \psi_j^*) \psi_i (\hat{\mathbf{e}}_p \cdot \nabla_t \ln n^2) \, dx \, dy = 0. \end{aligned} \quad (S15)$$

This equation can be expressed in a matrix form as $\hat{B}^2 \mathbf{c} = \beta^2 \mathbf{c}$, where \mathbf{c} is a column vector of the coefficients c_{ip} and \hat{B}^2 is a $2N \times 2N$ matrix

$$\hat{B}^2 = \hat{B}_0^2 + k^2 \hat{M} - 2k^2 n_0^2 \rho \hat{X} - \hat{G}. \quad (S16)$$

Here the matrices $\hat{B}_0^2, \hat{M}, \hat{X}$ and \hat{G} are indexed by index pairs ip and jq and their entries are

$$(\hat{B}_0^2)_{jq,ip} = \delta_{ji} \delta_{qp} \beta_{0i}^2 \quad (S17)$$

$$(\hat{M})_{jq,ip} = \delta_{qp} \int_{\mathbb{R}^2} \Delta n^2 \psi_j^* \psi_i \, dx \, dy \quad (S18)$$

$$(\hat{X})_{jq,ip} = \delta_{qp} \int_{\mathbb{R}^2} x \psi_j^* \psi_i \, dx \, dy \quad (S19)$$

$$(\hat{G})_{jq,ip} = \int_{\mathbb{R}^2} \hat{\mathbf{e}}_q \cdot (\nabla_t \psi_j^*) \psi_i (\hat{\mathbf{e}}_p \cdot \nabla_t \ln n^2) \, dx \, dy. \quad (S20)$$

The effects of index perturbation, bending and spin-orbit interaction are described by the matrices \hat{M}, \hat{X} and \hat{G} , respectively.

To employ our calculation practically, we calculate, for a given fibre, first the scalar modes and their propagation constants β_{0i} . We then numerically calculate the matrices $\hat{B}_0^2, \hat{M}, \hat{X}$ and \hat{G} . For a given curvature ρ , we then calculate the matrix \hat{B}^2 via Eq. S16 and subsequently its square root that we denote by $\hat{B} = (\hat{B}^2)^{1/2}$. Since the entries of the matrices \hat{M}, \hat{X} and \hat{G} are very small compared to the diagonal entries of \hat{B}_0^2 that are positive real numbers, such a matrix square root can be defined uniquely, taking the branch cut of the complex square root function along the negative real axis.

The matrix \hat{B} describes light propagation in the bent fibre with perturbed refractive index. In particular, the eigenvalues of \hat{B} are columns of coefficients $c_{jq,ip}$ that correspond to the modes of the fibre expressed as superpositions of our basis states. Moreover, the eigenvalues of \hat{B} describe the propagation constants of these modes. This way, the operator describing the evolution of the state in the fibre of length l can simply be expressed as $\hat{U}_\rho(l) = \exp(i\hat{B}l)$ in our basis.

To describe the evolution in the fibre that is not bent uniformly but whose curvature changes along its length, we divide it in a sufficient number of segments (in our calculations we used 100 segments), each of length Δl , the curvature in each of which can be regarded as constant. Then we simply multiply the matrices $\hat{U}_\rho(\Delta l)$ for the subsequent segments, which yields the total evolution operator.

In our experiments the fibre was bent in different directions, not just the x direction. To describe bending in the direction that makes an angle θ with the x axis, we must replace the matrix \hat{X} of Eq. S19 by a matrix \hat{X}_θ defined analogously, but with x replaced by $x_\theta = x \cos \theta + y \sin \theta$ in Eq. S19. The matrix \hat{X}_θ can be obtained from the matrix \hat{X} by employing the rotation operator \hat{R}_θ that rotates any state by the angle θ , such that $\hat{X}_\theta = \hat{R}_\theta \hat{X} \hat{R}_\theta^\dagger$.

In our experiments we worked with circularly polarised states rather than linearly polarised ones, while the calculation above employs the latter basis for the sake of simplicity. Transforming any matrix from one basis to the other is given by a simple similarity transformation.

2. Influence of odd and even perturbations of the refractive index on the modes

For a ‘naïve’ ray-optics based explanation of this phenomenon, see Supplementary movie SM5.

As we have shown, refractive index perturbation Δn^2 influence the modes via the matrix elements $(\hat{M})_{jq,ip}$ given by Eq. (S18) while fibre bending is related to the elements $(\hat{X})_{jq,ip}$ of Eq. (S19). To see some specific features of the situation when both the index perturbation and bending are present, we use a slightly different approach.

To do this, we consider an unperturbed fibre bent in the positive x direction as the starting point, and add the index perturbation on top of that. Then we can repeat the procedure described in Sec.1 of this document, but with the modes of a straight fibre ψ_i replaced by the modes of a bent fibre that we can denote by ψ'_i . The effect of the index perturbation will then be described by matrix elements analogous to Eq. (S18):

$$\hat{M}'_{jq,ip} = \delta_{pq} \int_{\mathbb{R}^2} \psi_j'^*(x, y) \psi_i'(x, y) \Delta n^2 \, dx \, dy. \quad (S21)$$

As it is well known², the modes are, with a good precision, the same as the modes of a straight fibre, just shifted by a certain distance Δx in the negative x direction (i.e., toward the outer side of the bend), so we can write approximately

$$\psi_i'(x, y) = \psi_i(x + \Delta x, y) \approx \psi_i(x, y) + \frac{\partial \psi_i(x, y)}{\partial x} \Delta x. \quad (S22)$$

To shorten the notation, we denote the product that appears in Eq. (S21) as

$$\rho'_{ji}(x, y) \equiv \psi_j'^*(x, y) \psi_i'(x, y), \quad (S23)$$

for which we can write a similar equation as (S22):

$$\rho'_{ji}(x, y) = \rho_{ji}(x, y) + \frac{\partial \rho_{ji}(x, y)}{\partial x} \Delta x, \quad (S24)$$

where $\rho_{ji}(x, y) \equiv \psi_j^*(x, y) \psi_i'(x, y)$ corresponds to the modes of a straight fibre.

Now we investigate the effect of adding the index perturbation to the ideal bent fibre. For a weak perturbation, the first order perturbation theory provides a good approximation. In the nondegenerate case, the perturbation corrections to the squared propagation constants would simply be described by diagonal elements of the matrix M' multiplied by k^2 ; however, in the ideal parabolic fibre, even when it is bent, there is a strong degeneracy of the modes, and one must diagonalise the perturbation within the degenerate subspaces first. This corresponds to choosing the “right” eigenvectors from the degenerate subspaces to which the actual bent fibre modes converge when the index perturbation gradually weakens and finally disappears. Without loss of generality, we can assume that the modes ψ'_i (and similarly their straight-fibre counterparts ψ_i) have already been chosen this way. Then, the deviations of squared propagation constants β^2 ,

compared to the situation without index perturbation, correspond to the diagonal elements of the matrix M' multiplied by k^2 similarly as in the non-degenerate case.

We can now evaluate these diagonal matrix elements corresponding to a bent perturbed fibre. To do that, we substitute Eq. (S24) into Eq. (S21):

$$M'_{iq,ip} = \delta_{pq} \int_{\mathbb{R}^2} \rho'_{ii}(x, y) \Delta n^2(x, y) dx dy = M'^{(0)}_{iq,ip} + \Delta x \delta_{pq} \int_{\mathbb{R}^2} \frac{\partial \rho_{ii}(x, y)}{\partial x} \Delta n^2(x, y) dx dy. \quad (S25)$$

Here $M'^{(0)}_{iq,ip}$ is the matrix element of the index perturbation evaluated for the straight fibre. We will now compare the effect of the perturbation for bent fibre with its effect for the straight fibre; the difference between the two effects is given by the term with the integral on the RHS of Eq. (S25). In the ideal parabolic fibre, the scalar propagation constants depend only on the combination $|l| + 2p$ of the mode indexes l (the angular momentum index) and p (the radial function index)². This means that the l indexes for the degenerate modes always differ by an even number, so each of the modes ψ_i contains only components of the same parity of l . Since the angular part of the mode with a given l , i.e., $e^{il\phi}$, is an odd function for l odd and an even function for l even, we see that each “right mode” ψ_i must be an even function for l even (i.e., $\psi_i(-x, -y) = \psi_i(x, y)$) and an odd function for l odd (i.e., $\psi_i(-x, -y) = -\psi_i(x, y)$). Consequently, $\rho_{ii}(x, y)$ must always be an even function and the partial derivative in Eq. (S25) must hence be an odd function.

Now assume that the index perturbation $\Delta n^2(x, y)$ is even, i.e. $\Delta n^2(-x, -y) = \Delta n^2(x, y)$. The function in the integral in Eq. (S25) is then an odd function because it is a product of an odd and even function. The integral therefore vanishes and we find that $M'_{iq,ip} = M'^{(0)}_{iq,ip}$. This means that the effect of an even perturbation on the bent fibre described by $M'_{iq,ip}$ is essentially the same as the effect of the perturbation on the straight fibre described by $M'^{(0)}_{iq,ip}$. Note that this does not mean that there would be no effect of the even perturbation on the fibre modes. The effect does exist, but since we are calibrating the perturbed (albeit straight) fibre, the imaging is not degraded. If, on the other hand, the function $\Delta n^2(x, y)$ is odd, i.e. $\Delta n^2(-x, -y) = -\Delta n^2(x, y)$, then the integrand on the RHS of Eq. (S25) is an even function, and the integral is nonzero in general. Therefore, odd index perturbations have different effects on a bent and straight fibre, and hence they degrade the imaging upon bending.

3. Influence of fibre radius and NA

Eq. (S25) enables us to estimate how the influence of index perturbations changes when we change the fibre radius and numerical aperture. For this purpose, we perform integration by parts with respect to x in Eq. (S25), obtaining

$$\int_{\mathbb{R}^2} \frac{\partial \rho_{ii}}{\partial x} \Delta n^2 dx dy = \int_{\mathbb{R}^2} (\rho_{ii} \Delta n^2) \Big|_{x=-\infty}^{x=\infty} dy - \int_{\mathbb{R}^2} \rho_{ii} \frac{\partial \Delta n^2(x, y)}{\partial x} dx dy. \quad (S26)$$

Due to the exponential decay of the modes for large radii, the first term vanishes and only the second term remains, so we can rewrite Eq. (S25) as

$$M'_{iq,ip} - M'^{(0)}_{iq,ip} = -\delta_{pq} \Delta x \int_{\mathbb{R}^2} \rho_{ii} \frac{\partial \Delta n^2(x,y)}{\partial x} dx dy. \quad (S27)$$

Suppose now that the NA of the fibre is fixed and the radius R is varied while the index perturbation keeps its functional form (e.g., it is one of the Zernike functions) that is spread over the fibre radius R ; in other words, the perturbation can be expressed as $\Delta n^2(x,y) = f\left(\frac{x}{R}, \frac{y}{R}\right)$, where f is a fixed function. Then the partial derivative $\frac{\partial \Delta n^2(x,y)}{\partial x}$ in Eq. (S25) scales like R^{-1} and since the modes are normalised, $\int_{\mathbb{R}^2} \rho_{ii} dx dy = 1$, so does scale the whole integral. On the other hand, if we instead fix the fibre radius R and change the numerical aperture, the partial derivative $\frac{\partial \Delta n^2(x,y)}{\partial x}$ does not change, so the integral in Eq. (S27) changes either. The last thing that remains to take into account is the dependence on R and NA of the mode shift Δx caused by the bending. It can be shown² that the shift is given approximately by $\Delta x = \rho b^2 = \frac{\rho n_0^2 R^2}{NA^2}$. Combining in Eq. (S27) the dependences on R and NA of Δx and the integral, we get

$$M'_{iq,ip} - M'^{(0)}_{iq,ip} \propto \frac{R^2}{NA^2} \frac{1}{R} = \frac{R}{NA^2}.$$

This way, the index perturbation influence on imaging performance scales proportionally to the fibre radius and inversely proportionally to the square of the fibre numerical aperture.

4. Adiabatic shapes of fibre probe under bending

In our experiments we used fibre shapes for which the curvature changes smoothly all the way from proximal to distal end. This way the fibre modes that are influenced by the fibre curvature change smoothly as well and the state of light adiabatically adapts to the changing conditions. The imaging performance is therefore less degraded than for non-adiabatic changes of the curvature, which is desirable.

Since both fibre ends are inserted in rigid ferrules, the curvature at the ends is zero. We therefore look for an equilibrium fibre shape satisfying these boundary conditions, which corresponds to zero torque within the fibre at the ends. To find the fibre shape, we follow the procedure described in Ref. [3]. We assume that the deformation occurs only in one plane which we take as the xy plane, and that the force \vec{F} with which adjacent elements of the fibre act on each other is oriented along the x axis.

Further, let θ denote the angle between the axis of a fibre element located at the point (x,y) and the x axis, E and I denote the Young elastic module and the moment of inertia of the fibre cross section (i.e., a disk), respectively, and let l be the length measured along the fibre. We then arrive at the following differential equation³ for θ ,

$$EI \frac{d^2\theta}{dl^2} - F \sin \theta = 0. \quad (S28)$$

This equation, when multiplied by $d\theta/dl$, can be integrated to obtain $EI (d\theta/dl)^2/2 + F\cos \theta = A$, where A is a constant. From this we express the derivative

$$\frac{d\theta}{dl} = \sqrt{\frac{2(A - F\cos \theta)}{EI}} \quad (S29)$$

that expresses the curvature and has to be zero at both ends of the bent fibre segment, which implies that $A = F\cos \theta$ (at both ends), i.e., at $l = 0$ and $l = L$, where L is the total length of the fibre segment between the ferrules, which experiences bending. If we denote by θ_0 the value of θ corresponding to $l = 0$, we can write $\theta_0 = \arccos(A/F)$, and the length of the fibre is

$$L = \sqrt{\frac{EI}{2}} \int_{\theta_0}^{2\pi - \theta_0} \frac{d\theta}{\sqrt{A - F\cos \theta}} = \sqrt{\frac{EI}{2F}} \int_{\theta_0}^{2\pi - \theta_0} \frac{d\theta}{\sqrt{\cos \theta_0 - \cos \theta}}. \quad (S30)$$

The upper limit $2\pi - \theta_0$ corresponds to the smallest value of $\theta > \theta_0$ where the zero-curvature condition, $A = F\cos \theta$, is again satisfied. This way, the angle between the directions of the fibre at its two ends is $\Delta\theta = 2\pi - \theta_0 - \theta_0 = 2(\pi - \theta_0)$.

Further, with the help of Eq. (S29) we can express the coordinates x, y as functions of θ , which describes the fibre shape parametrically:

$$x = \int_0^l \cos \theta \, dl = \sqrt{\frac{EI}{2F}} \int_{\theta_0}^{\theta} \frac{\cos \theta \, d\theta}{\sqrt{\cos \theta_0 - \cos \theta}}, \quad (S31)$$

and

$$y = \int_0^l \sin \theta \, dl = \sqrt{\frac{EI}{2F}} \int_{\theta_0}^{\theta} \frac{\sin \theta \, d\theta}{\sqrt{\cos \theta_0 - \cos \theta}} = \sqrt{\frac{2EI}{F}} \sqrt{\cos \theta_0 - \cos \theta}. \quad (S32)$$

These equations fully determine the fibre shape in a parametric way, but they still contain constants E, I, F that might not be easy to access experimentally. However, in an experiment we can easily access the fibre length L and the angle $\Delta\theta$ defined above. To employ them, we first calculate θ_0 from the known $\Delta\theta$ and evaluate the integral in Eq. (S30) which, together with the known value of L , determines the constant $\sqrt{EI/F}$. Equipped with its value, we solve equation (S28) numerically to determine the function θ_l , and subsequently use the parametric equations (S31) and (S32) to find the fibre shape $(x(\theta), y(\theta))$ as well as the fibre curvature as a function of the length along the fibre, l , which is then useful for numerical simulations. Fig. S1 shows fibre shapes for $\Delta\theta$ ranging from zero to π in both directions.

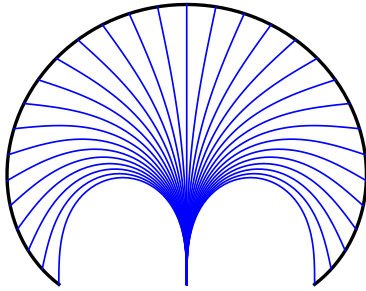


Figure S1: Fibre shapes corresponding to zero curvature at both ends for $\Delta\theta$ ranging from zero to π in both directions. The curves were subsequently rotated so that the proximal end always points in the same direction (here vertically), which also corresponds to our experimental setup. The black curve marks the positions of the distal end for different $\Delta\theta$.

5. Simulation of the Refractive Index perturbations on imaging performance

Here we explore the influence of various types of refractive index perturbations on the imaging performance of the bent fibre. The simulation is analogous to that of the manuscript, i.e. we propagate through bent fibre the light fields that would lead to perfect foci in the straight fibre. These foci are used to image (raster scan) periodic sinusoidal gratings to reconstruct the contrast transfer function, which is then used to identify the resolution and estimate the resulting imaging capacity. The fibre features specifications of GI_M^2 and it is adiabatically bent to 90 degrees. The fibre's n^2 is considered as perfectly parabolic with a perturbation defined by a single Zernike polynomial. The polynomial is normalised so that $\int_0^R \int_0^{2\pi} \frac{r}{R^2} Z_m^n \left(\frac{r}{R}, \phi \right) dr d\phi = 1$, where R is the radius of the fibre core. Its magnitude is varied by a multiplicative factor, ranging between -10^{-3} and 10^{-3} (unitless as it describes changes to the n^2). The results are shown in Figure S2.

The first 'piston' (Z_0^0) term has not been studied, as it will not affect the bending resilience (the effect is identical in straight and bent fibres, and it would be accounted for during the calibration). The behaviour of the lower orders agrees with intuitive expectations: The linear n^2 slant, perpendicular to the bending direction (Z_1^{-1}), has no effect as it only shifts the light in the y direction. The linear n^2 slant, in the direction of the bending (Z_1^1), has the same effect as the bending itself. While negative values add to the bending effect and push the propagating light towards the core-cladding boundary where it suffers from attenuation and coupling between modes, the positive values counter-act the effect and prevent the signals from coupling and losses. The parabolic term (Z_2^0) is identical with the n^2 profile of the ideal fibre, its negative values thereby effectively increase the fibre's NA which leads to an increase in the imaging capacity (higher NAs are more immune to potential slant due to bending, the off-axis displacement of the potential well is smaller).

With higher orders, the observations exhibit a stark contrast between the aberrations of the even orders - antisymmetric with respect to the axis, and the odd orders - symmetric with respect to the axis), which follows the expectation derived above in Materials and Methods, Section 2.

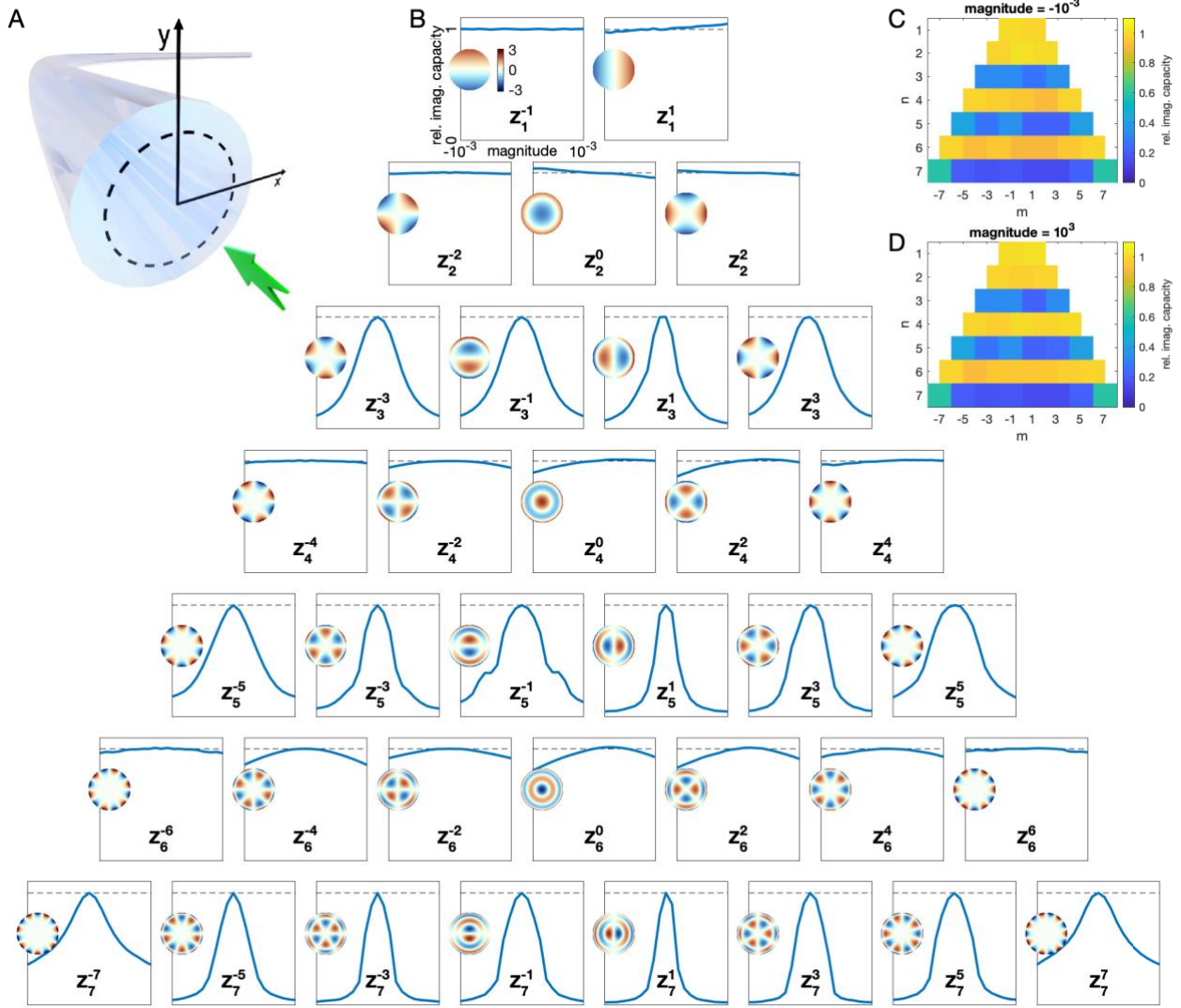


Fig. S2. Bending resilience of imaging for fibres featuring various aberrations in n^2 profile. **A**, The considered geometry of 34 mm long segment bent adiabatically to 90°. **B**, Relative imaging capacities (with respect to unperturbed fibre, core diameter of 50 μm , NA of 0.29) for aberrations described by Zernike polynomials, as functions of perturbation magnitude. **C** and **D**, Relative imaging capacities for the lowest and the highest refractive index aberration magnitude studied.

6. Assessment of the Refractive Index of the used fibres

Profiles of optical refractive index for the fibres utilised in this work in both experimental and simulation parts were obtained via IFA-100 Multiwavelength Optical Fiber Analyzer from Interfiber Analysis. By scanning the fibre probe under-test from the side, recording the relative phase and tomographic reconstruction methods, the device for optical refractive index profile measurements with claimed minimal detectable index fluctuations at the level of $n = \pm 0.0001$. All measurements were carried out at a wavelength of 632nm, during tomographic imaging the fibre was rotated over 180° with steps of 5°^{4,5}. The perturbations Δn^2 to perfectly parabolic profile of n^2 , identified by this procedure, are summarized in Figs. S3 – S6, also isolating their antisymmetric and symmetric contributions.

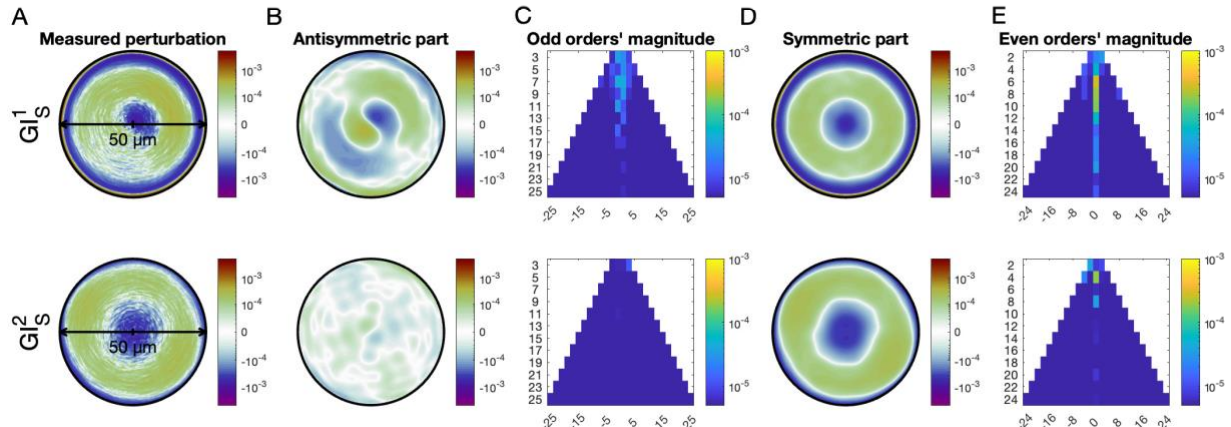


Fig. S3. Analysis of the refractive index profiles for GI fibers. **A**, the difference of the measured n^2 and the ideal parabolic shape of the best fit across the core area (diameter was set based on the manufacturer's specifications). Note the highly nonlinear false color representation shown in the colorbar. **B**, Antisymmetric part of the aberration composed of the odd orders of the Zernike polynomial basis. **C**, magnitude (absolute value) of the odd Zernike polynomials. **D**, Symmetric part of the aberration composed of the even orders of the Zernike polynomial basis. **E**, magnitude of the even Zernike polynomials.

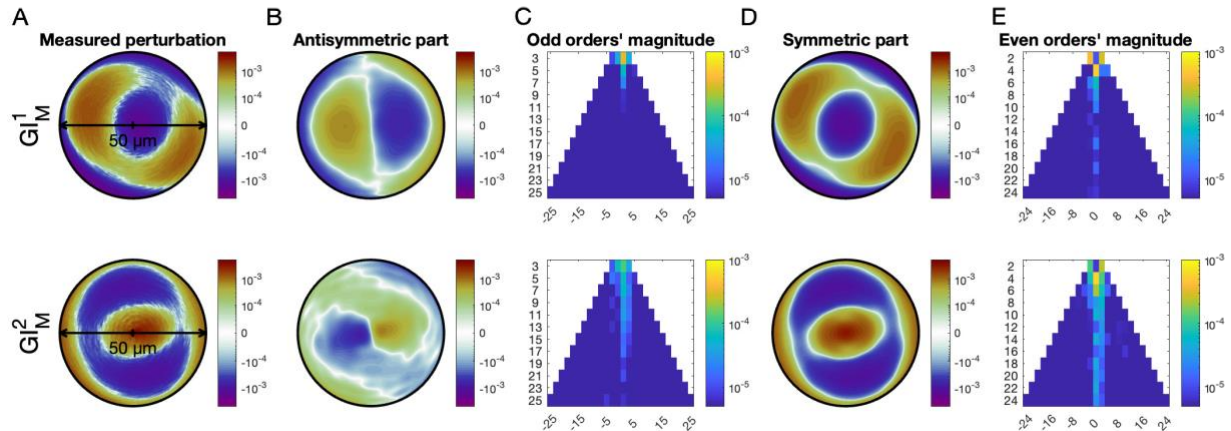


Fig. S4. Analysis of the refractive index profiles for GI_M fibers. The organisation of the figure is identical to that of Fig. S3.

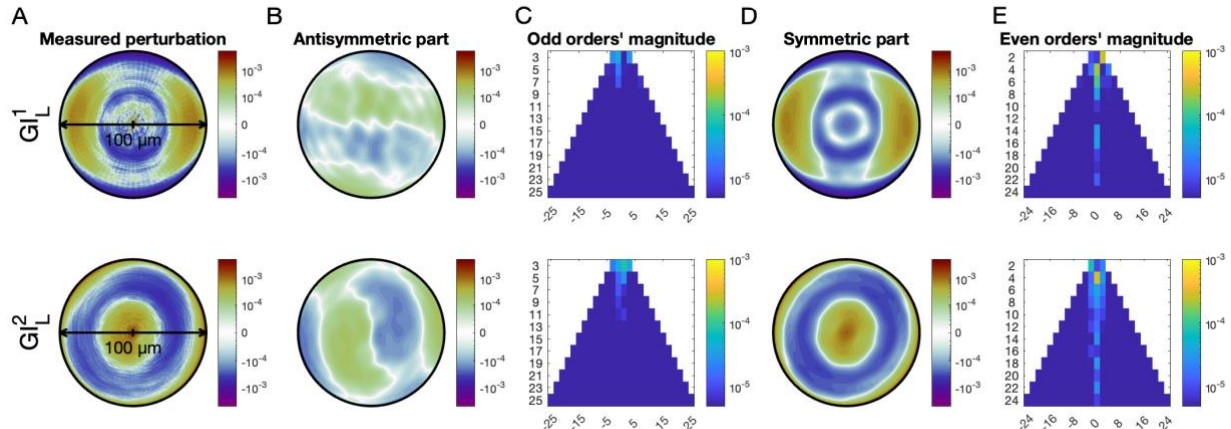


Fig. S5. Analysis of the refractive index profiles for GI_L fibres. The organisation of the figure is identical to that of Fig. S3.

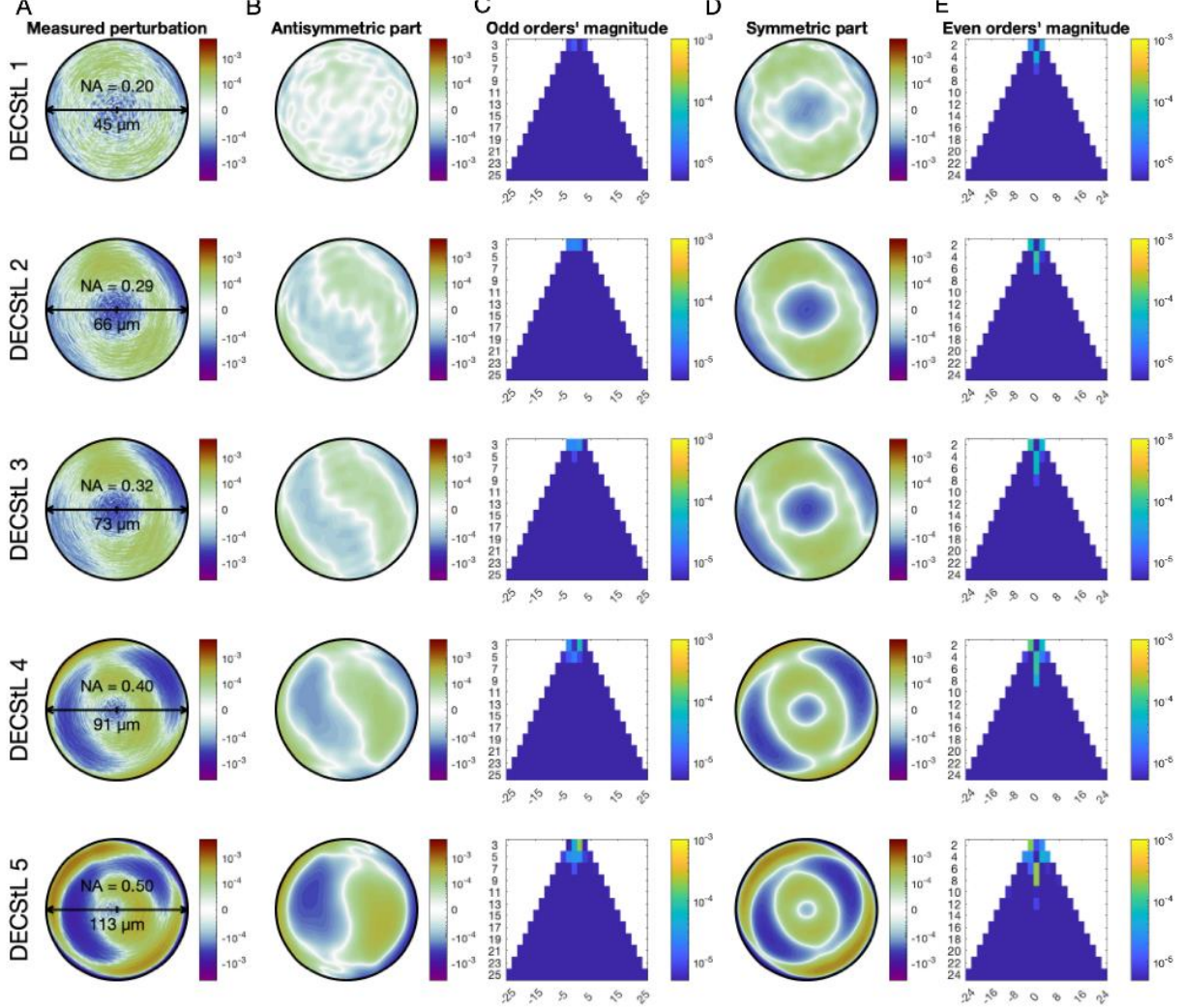


Fig. S6. Analysis of the refractive index profiles for the DECSL waveguide. The organisation of the figure is identical to that of Fig. S3. Individual rows shows different levels of truncation in virtual core size and NA, accordingly to Fig. 3.

7. Simple metric for course bending resilience estimation

As explained above in section 3, the influence of Δn^2 perturbation grows with the core radius R and falls with the square of the NA. It is also the mainly the asymmetric part of Δn^2 , causing the image degradation, as explained in section 2. Therefore, here we attempt to establish, whether and to what extent, the bending resilience can be estimated purely from the magnitude of this perturbation and the parameters of the fibre, without the necessity of the complete, and very computationally intensive mathematical algorithms used in this study. The simplest possible quantity would be the radius and NA regularised absolute value of Δn^2 , averaged over the core of the fibre: $\langle \left| \frac{\Delta n^2 R}{NA^2} \right| \rangle$, which we refer to here as the bending resilience predictor (BRP). Figure S7 presents the relative decline of imaging capacity upon bending (the imaging capacity at $\epsilon = 90^\circ$

over the imaging capacity at the initial straight state where calibration took place) against the corresponding BRP, for experimentally obtained as well as simulated results from our studies. As the ‘rule of thumb’ we can state that when BRP remains below the value of $5 \cdot 10^{-3} \mu\text{m}$ there is a good chance of bending resilience at least for applications involving imaging using 10s of cm long segments of fibre.

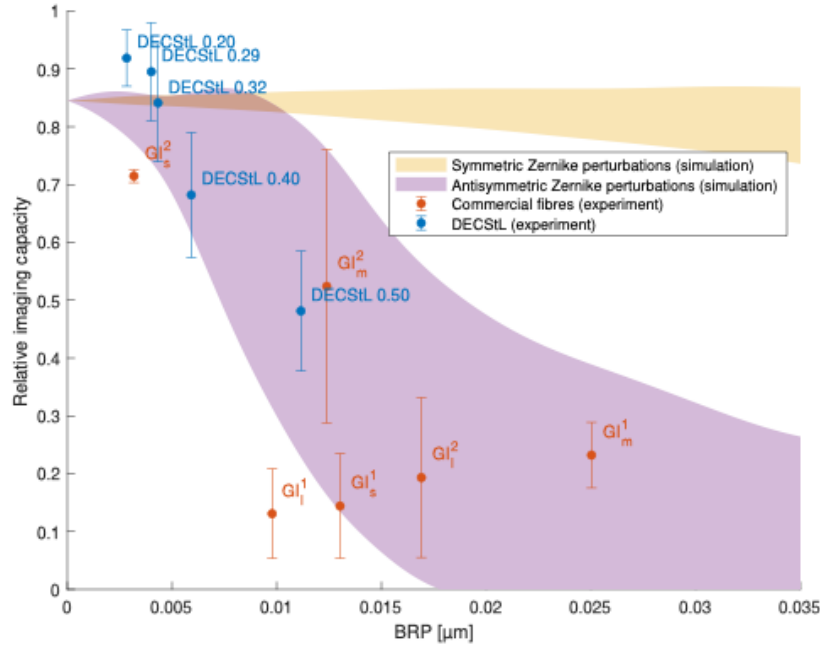


Fig. S7. Relative imaging capacity at $\epsilon = 90^\circ$ as a function of bending resilience predictor. The shaded zones are single standard deviation wide confidence intervals obtained from simulations shown in Fig. S2. The points show the experimental data on commercial fibres and truncated DECStL, the corresponding error bars show the single standard deviation spread for the six roll orientations.

Note that the simulated data (for parameters of the GI_M^2 fibre) show the relative imaging capacity at zero BRP (no Δn^2 perturbations) of ≈ 0.84 . This drop is caused by the transported light being displaced from the core due to the bending and a fraction of the signal, which penetrated to the cladding, has been decoupled. The same effect is present in all our fibres and it becomes stronger for shallower potential wells, i.e. smaller NA and larger core. This effect however does not occur in the truncated measurements of the DECStL waveguide as we can trim its core area and NA only virtually at its extremities but not inside.

8. Fabrication of DECStL waveguides

The GRIN rods were fabricated by a silver-sodium based two-step ion exchange process in 125 μm rods of a patented glass composition⁶. For that, a polished cylindrical preform of this glass composition was fabricated by grinding and polishing before it was drawn to 125 μm diameter in a fibre drawing tower at temperatures of about 1000 $^\circ\text{C}$. In a first ion exchange step, pieces of 60 mm length were immersed in a salt bath of a mixture of silver, sodium and potassium nitrate with a 20 % silver nitrate content. By this, around 90% of all sodium ions in the glass were replaced by silver ions leading to a high silver containing glass of homogenously increased refractive index of

about 1.64. In a second ion exchange step, these rods were subsequently placed in a sodium-potassium nitrate mixture to initiate a reverse out-diffusion process of silver ions from the surface of the glass rods, which are again replaced by sodium ions. This procedure results in the desired radial parabolic index profile of a numerical aperture of 0.5 and the maximum index at the centre of the rods.

9. Experimental Setup

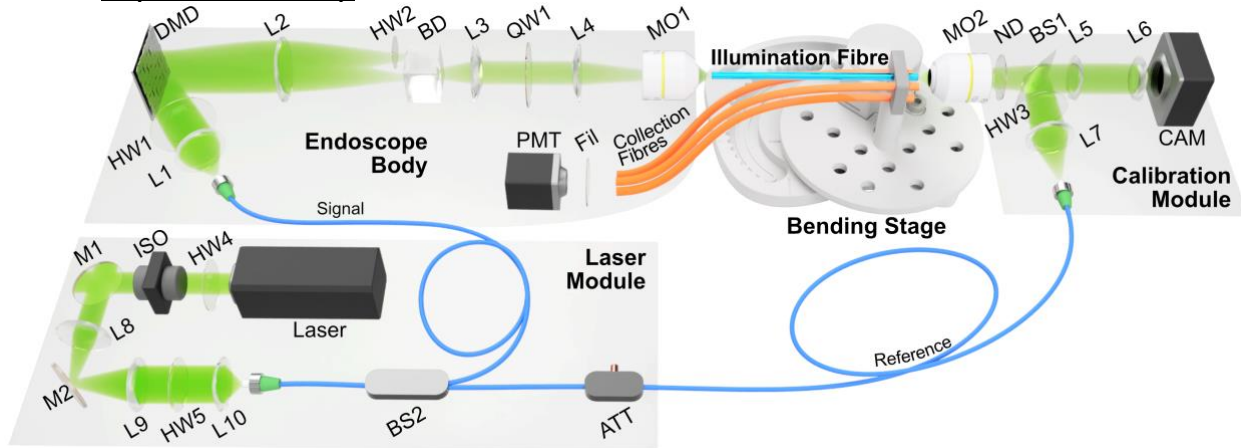


Fig. S7. Schematic representation of the experimental setup. Upon measurement of transmission matrix, the calibration module can be removed, and endoscope is ready for imaging. Specialised assemblies providing bending and rotational degrees of freedom for positioning fibre probes under test are presented in the Fig. S8 in greater details.

The linearly polarised light emitted by a single-frequency laser source (Coherent Sapphire 532 SF NX) at the 532 nm wavelength is coupled into the polarisation-maintaining fibre via lens assembly L8-10 and HW5 as depicted in Fig. S7. Subsequent fibre beamsplitter BS2 divides the coupled light into signal and reference arm with 99:1 ratio. The overall optical power in the system is controlled using HW4 placed before optical isolator ISO, while the power in the reference beam can be tuned independently by the MEMS-based fibre attenuator (ATT).

Two pairs of lenses, L2+L3 and L4+MO1, aligned in 4-f configuration, relay the DMD plane to the proximal fibre facet with appropriate demagnification. The demagnification of 80 times was chosen to closely match the linear size of the DMD active area (768 pixels x 13.69 μm pitch) to the core diameter of the largest probe employed in this study (DECStL, 125 μm). For the fibre types of a smaller core, the active area of the DMD was shrunk, allowing to match the core size and enable faster frame rates exceeding 30,000 FPS for the 50 μm core probes.

The input fields used for calibration are truncated plane waves coupled to the fibre at different incidence angles within the acceptance angle of the fibre defined by its NA. Such basis can be spatially resolved in the Fourier plane and represents an orthogonal grid of diffraction-limited foci, which can be steered across by changing the carrier frequency of the DMD gratings. In this work, two distantly spaced regions of the DMD Fourier plane were used to split illumination power into two beams. One of the beams passes through the half-wave plate HW2, changing polarisation to the orthogonal state and gets merged with another beam by polarisation beam displacer BD. Similarly to the previous work⁷, this scheme allows gaining independent control over two orthogonal polarisation states of the light coupled to the fibre. The focal length of L2 and the

position of the beams in the Fourier plane are chosen to match the required beam separation of 4mm for the displacer BD.

The calibration module optical scheme consisting of microscope objective MO2 and a pair of lenses L5-6 is designed to image the far-field plane of the distal fibre facet onto a camera CAM. The reference beam delivered to the module by a polarisation maintaining fibre is collimated by the L7 and demagnified by the L5-L6 lens pair. Half-wave plate HW3 (Thorlabs WPMH10M-532) rotates the angle of polarisation of the phase reference beam, allowing to maximise interference contrast at CAM.

10. Design of the Bending Stage

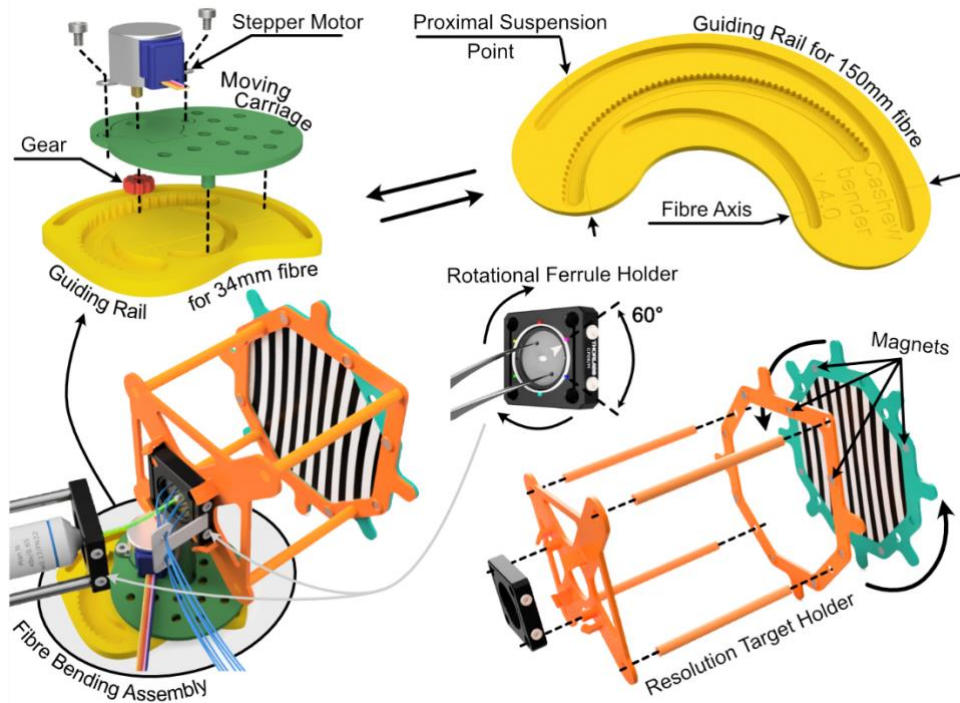


Fig. S8. 3D printed bending assemblies allowing for performing bending, twisting deformations as well as imaging resolution Ronchi targets. Designs related to waveguide bending are available as supplementary Data S1.

11. Fibre length influence on bending resilience

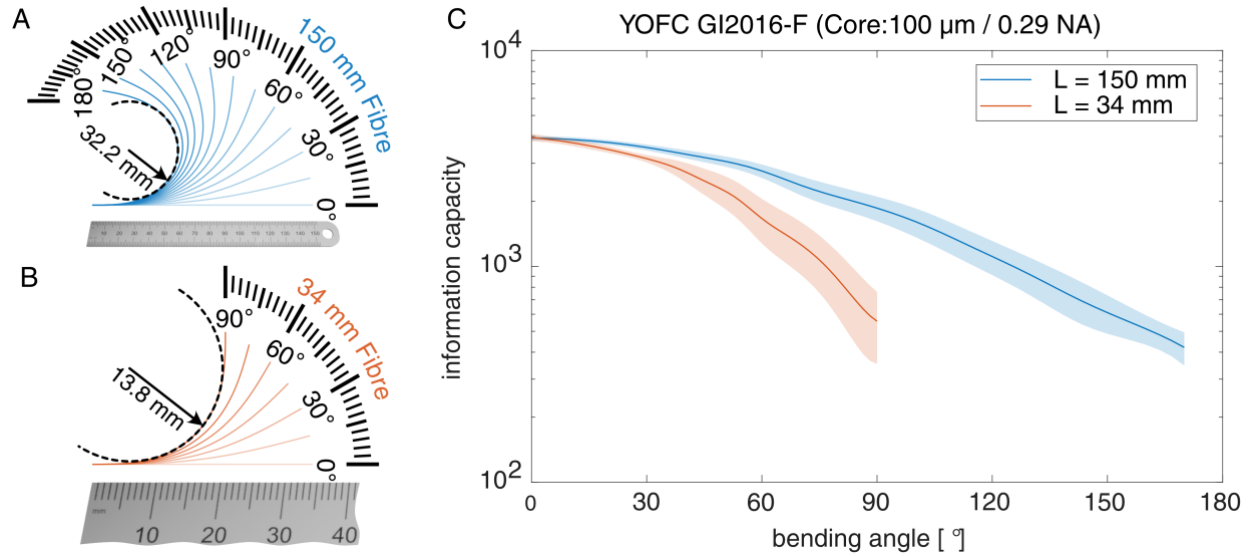


Fig. S9. Comparison of the under-bend imaging performance for two segments of the GI_L^2 fibre (YOFC GI2016-F), which, however, differ in length. **A** and **B**, Bending layouts for both long (150mm) and short (34mm) fibre probes. **C**, Trends on bending resilience for two fibre pieces of different lengths confirm utilising longer fibres with restricted bending radii as a preferable way to minimise overall performance degradation. Error bars represent the standard deviation of imaging capacity resulted from the resolution target measurements taken for different rotational orientations of the fibre probe.

Fibre ID	Manufacturer	Fibre Type	Profile	Core Size (μm)	Numerical aperture
SI	Thorlabs	FG050UGA	STEP	50 ± 1	0.22 ± 0.02
GI_S^1	Corning	ClearCurve (OM5)	GRIN	50 ± 2.5	0.200 ± 0.015
GI_S^2	Prismian Group	DRAKA WideCap (OM5)	GRIN	50 ± 2.5	0.200 ± 0.015
GI_M^1	Prismian Group	DrakaElite 50/80um	GRIN	50 ± 2	0.290 ± 0.015
GI_M^2	YOFC	GI2016-C	GRIN	50 ± 3	0.29 ± 0.02
GI_L^1	Prismian Group	DrakaElite 100/140um	GRIN	100 ± 4	0.290 ± 0.015
GI_L^2	YOFC	GI2016-F	GRIN	100 ± 3	0.29 ± 0.02
DECStL	GrinTECH	custom	GRIN	~ 125	~ 0.5

Table S1: List of the fibres utilised in the studies with a set of primary parameters specified by manufacturers.



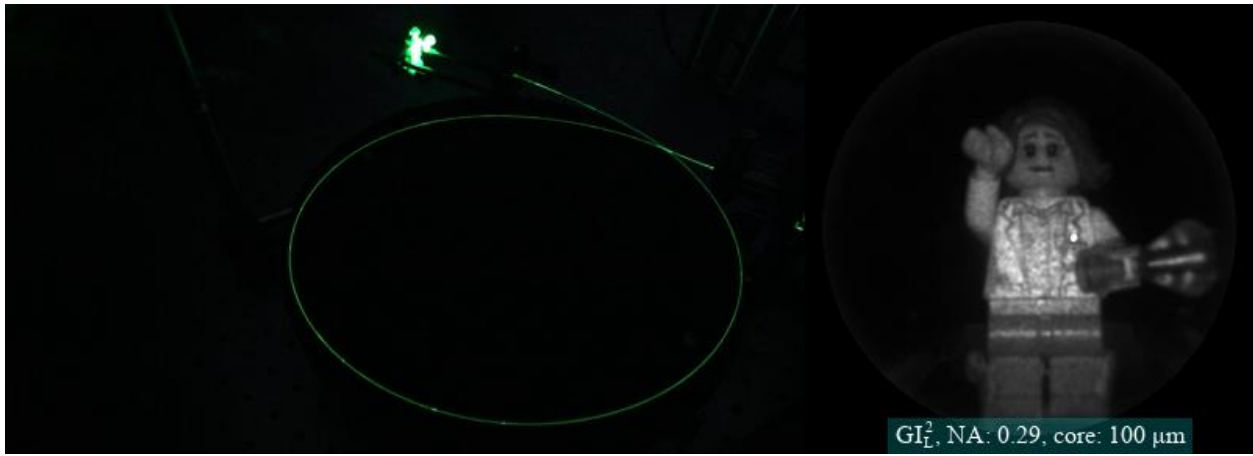
Movie SM1: Recordings of the scene during progressing bending deformation performed for the probes type under test. The probes of 34mm were bent from straight position to 90 degrees angle, which correspond to a maximum curvature radius of 13.8mm. For the fibres with significant difference of imaging performance on roll orientation both the worst as well as the best recordings are displayed.

Movie available from <https://zenodo.org/records/18086670/files/SM1.mp4?download=1>.

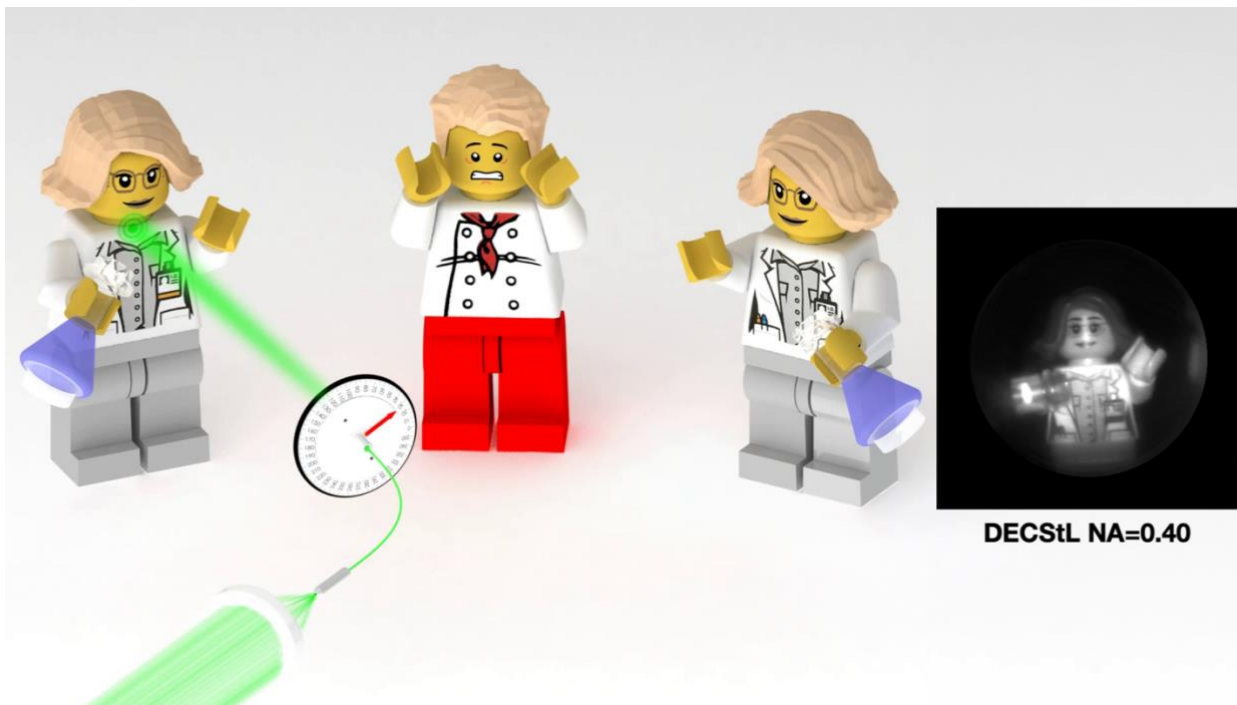


Movie SM2: Recording of the static scene containing a single Lego figurine while fibre experiencing pronounced bending deformations, mimicking fully flexible endoscope operation. The probe of GI_s^2 fibre type is 1m long. This fibre type demonstrated one of the best imaging performance resilience to bending deformation.

Movie available from <https://zenodo.org/records/18086670/files/SM2.mp4?download=1>.

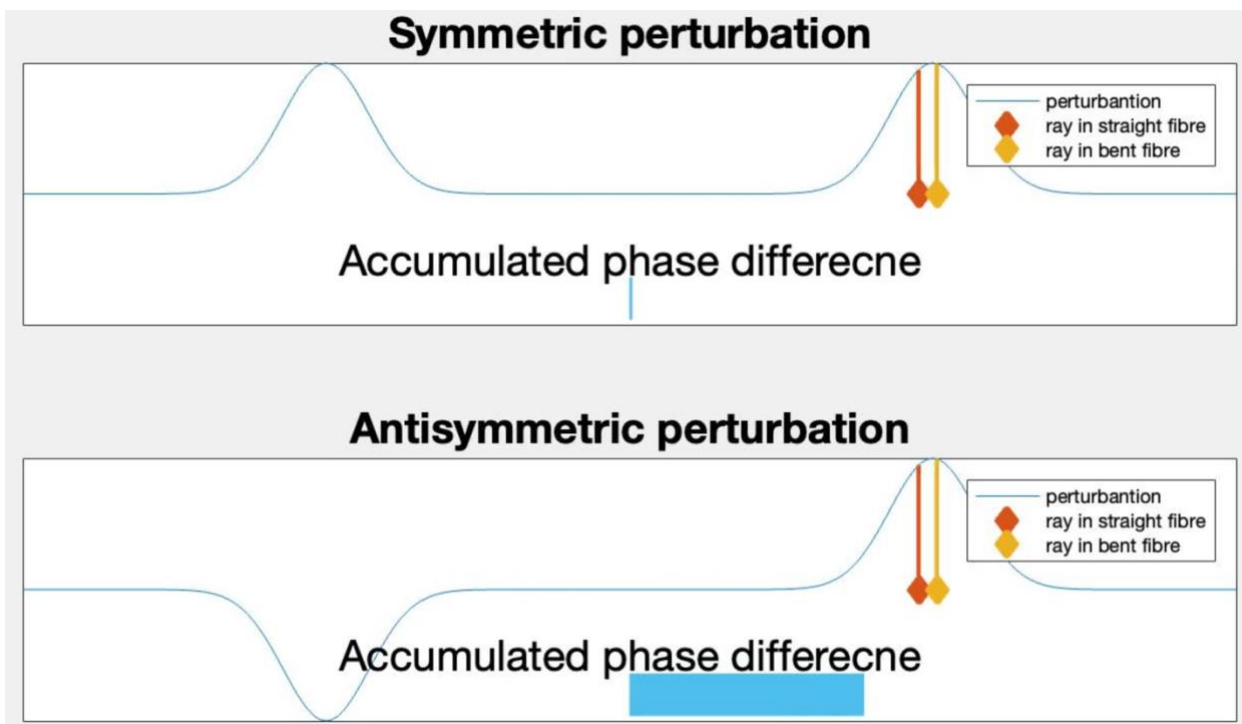


Movie SM3: Recording of the static scene containing a single Lego figurine while fibre experiencing pronounced bending deformations, mimicking fully flexible endoscope operation. The probe of GI_L^2 fibre type is 1m long. This fibre type demonstrated one of the best imaging performance resilience to bending deformation. Movie available from <https://zenodo.org/records/18086670/files/SM3.mp4?download=1>.



Movie SM4: Recordings of the scene during progressing twist deformation performed for the probes under test. Twisting of the distal end of the fibre probes was gradually changed from 0 to 30 degrees.

Movie available from <https://zenodo.org/records/18086670/files/SM4.mp4?download=1>.



Movie SM5: The ‘naïve’ explanation of the contrasting bending resilience of fibres suffering from symmetric and asymmetric perturbations Δn^2 , respectively. It derives from the fact that rays coupled into the fibre periodically visit the opposite sides of the core. When fibre is bent, the rays get displaced towards the outer side of the curved segment and are exposed to the influence of the perturbation causing a shift in the rays’ phases. In case the perturbation is symmetric (even), its spatial derivative is odd, thereby the ray loses close to the same amount of phase on one side as what it has acquired on the opposite side previously, thereby cancelling both contributions. If the perturbation is, however, odd, its derivative is even, thereby the ray acquires similar amount of phase on both sides which accumulates along the whole propagation throughout the bend. Movie available from <https://zenodo.org/records/18086670/files/SM5.mp4?download=1>

Data S1 (separate file - FibreBendingDesigns.zip): 3-D models for bending apparatus.

The attached archive contains .stl files for 3D printed components used in this work for fibre bending. Files are named following nomenclature at Figure S8. Resource available from <https://zenodo.org/records/18086670/files/FibreBendingDesigns.zip?download=1>

References:

1. Snyder, A. W., Love, J. D. & others. *Optical waveguide theory*. vol. 175 (Chapman and hall London, 1983).
2. Flaes, D. E. B. *et al.* Robustness of light-transport processes to bending deformations in graded-index multimode waveguides. *Phys Rev Lett* **120**, 233901 (2018).
3. Landau, L. D., Lifshitz, E. M., Kosevich, A. M. & Pitaevskii, L. P. *Theory of elasticity: volume 7*. vol. 7 (Elsevier, 1986).
4. Yablon, A. D. Multi-wavelength optical fiber refractive index profiling by spatially resolved Fourier transform spectroscopy. *Journal of Lightwave Technology* **28**, 360–364 (2009).
5. Yablon, A. D. Multifocus tomographic algorithm for measuring optically thick specimens. *Opt Lett* **38**, 4393–4396 (2013).
6. Bernhard Messerschmidt *et al.* Alumino-boro-silicate glass and process to make crystal-free Gradient Index Lenses, *EP Patent*, EP1544176A2 (2004).
7. Gomes, A. D., Turtaev, S., Du, Y. & Čižmár, T. Near perfect focusing through multimode fibres. *Opt Express* **30**, 10645–10663 (2022).